

AD-A125 884

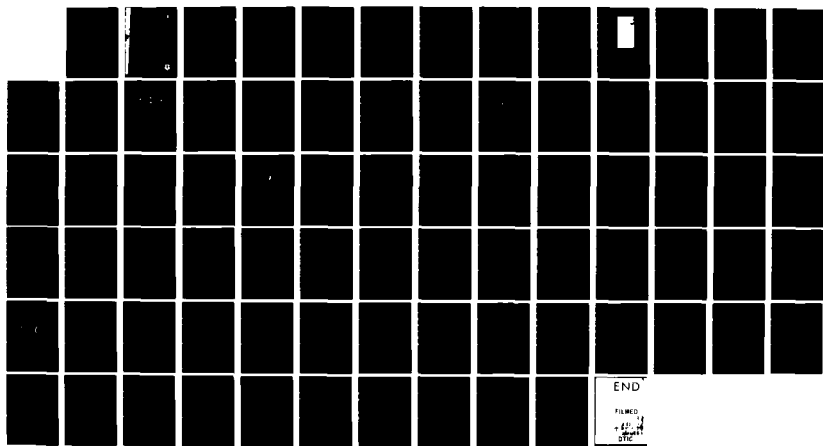
MAGNETOSPHERIC AND HIGH-LATITUDE IONOSPHERIC
ELECTRODYNAMICS(U) AIR FORCE GEOPHYSICS LAB HANSCOM AFB
MA W J BURKE ET AL. 13 APR 82 AFGL-TR-82-0131

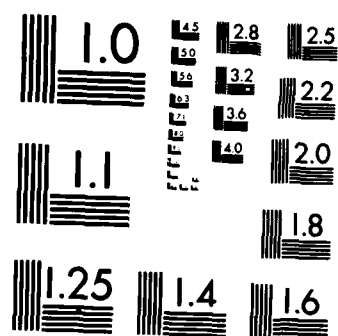
1/1

UNCLASSIFIED

F/G 4/1

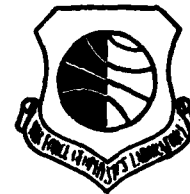
NL





MICROCOPY RESOLUTION TEST CHART
NATIONAL BUREAU OF STANDARDS-1963-A

AFGL-TR-82-0131
AIR FORCE SURVEYS IN GEOPHYSICS, NO. 430



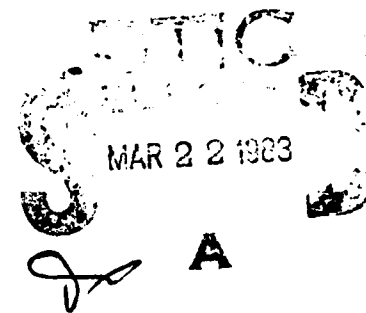
ADA 125884

**Magnetospheric and High-Latitude
Ionospheric Electrodynamics**

**WILLIAM J. BURKE
DAVID A. HARDY
ROGER P. VANCOUR**

13 April 1982

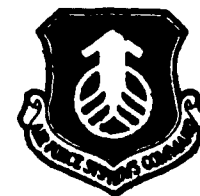
Approved for public release; distribution unlimited.



DTIC FILE COPY

**SPACE PHYSICS DIVISION PROJECT 2311
AIR FORCE GEOPHYSICS LABORATORY
HANSCOM AFB, MASSACHUSETTS 01731**

AIR FORCE SYSTEMS COMMAND, USAF



83 03 22 040

This report has been reviewed by the ESD Public Affairs Office (PA)
and is releasable to the National Technical Information Service (NTIS).

This technical report has been reviewed and
is approved for publication.

Alva T. Stair, Jr.

DR. ALVA T. STAIR, Jr
Chief Scientist

Qualified requestors may obtain additional copies from the
Defense Technical Information Center. All others should apply
to the National Technical Information Service.

Unclassified

SECURITY CLASSIFICATION OF THIS PAGE (When Data Entered)

REPORT DOCUMENTATION PAGE		READ INSTRUCTIONS BEFORE COMPLETING FORM
1. REPORT NUMBER AFGL-TR-82-0131	2. GOVT ACCESSION NO.	3. RECIPIENT'S CATALOG NUMBER
4. TITLE (and Subtitle) MAGNETOSPHERIC AND HIGH-LATITUDE IONOSPHERIC ELECTRODYNAMICS		5. TYPE OF REPORT & PERIOD COVERED Scientific. Interim.
		6. PERFORMING ORG. REPORT NUMBER AFSG, No. 439
7. AUTHOR(s) William J. Burke David A. Hardy Roger P. Vancour		8. CONTRACT OR GRANT NUMBER(s)
9. PERFORMING ORGANIZATION NAME AND ADDRESS Air Force Geophysics Laboratory (PHG) Hanscom AFB Massachusetts 01731		10. PROGRAM ELEMENT, PROJECT, TASK AREA & WORK UNIT NUMBERS 2311G206 61102F
11. CONTROLLING OFFICE NAME AND ADDRESS Air Force Geophysics Laboratory (PHG) Hanscom AFB Massachusetts 01731		12. REPORT DATE 13 April 1982
		13. NUMBER OF PAGES 80
14. MONITORING AGENCY NAME & ADDRESS (if different from Controlling Office)		15. SECURITY CLASS. (of this report) Unclassified
		15a. DECLASSIFICATION DOWNGRADING SCHEDULE
16. DISTRIBUTION STATEMENT (of this Report) Approved for public release; distribution unlimited		
17. DISTRIBUTION STATEMENT (of the abstract entered in Block 20, if different from Report)		
18. SUPPLEMENTARY NOTES		
19. KEY WORDS (Continue on reverse side if necessary and identify by block number) Electrodynamics High-latitude ionosphere Auroral oval		
20. ABSTRACT (Continue on reverse side if necessary and identify by block number) This report provides an introductory overview of electrodynamic interactions between the magnetosphere and ionosphere. In the first half of the paper, the viscous interaction and magnetic merging models for driving convection are described. The notion of adiabatic heating as a natural consequence of convection is introduced, in conjunction with a quasi-empirical model for the magnetospheric potential. The second half of the paper concerns observations of electrodynamic quantities taken in the topside ionosphere in the polar cap and auroral oval.		

DD FORM 1 JAN 73 1473 EDITION OF 1 NOV 65 IS OBSOLETE

Unclassified
SECURITY CLASSIFICATION OF THIS PAGE (When Data Entered)



Contents

1. INTRODUCTION	7
2. MAGNETOSPHERIC BOUNDARY INTERACTIONS	10
2.1 The Magnetopause	10
2.2 Convection	13
2.3 Boundary Layers	17
3. THE PLASMA SHEET	20
3.1 Adiabatic Motion in the Plasma Sheet	23
3.2 Pitch Angle Diffusion of Plasma Sheet Particles	30
4. ELECTRICAL COUPLING OF THE MAGNETOSPHERE AND IONOSPHERE	34
5. HIGH-LATITUDE ELECTRIC FIELDS	36
6. POLAR CAP ELECTRODYNAMICS	39
6.1 Large-Scale Electric Field Patterns	40
6.2 Polar Cap Precipitation	46
6.3 Polar Cap Arcs	49
7. AURORAL OVAL ELECTRODYNAMICS	54
7.1 Global Field-Aligned Currents	54
7.2 The Equatorward Boundary of the Oval	56
7.3 Inverted-V Phenomenology	62
7.4 Substorms	66
8. CONCLUSIONS	68
SYMBOLS AND GLOSSARY	71
REFERENCES	75

Illustrations

1. DMSP Imagery From Over Western North America	9
2. Model of the Earth's Magnetic Field Distorted by the Solar Wind	12
3. Equatorial Projection of Convection Pattern in Viscous Interaction Model	14
4. Magnetic Field Geometry and Electric Field Required for Magnetic Merging	15
5. Snapshot of Magnetic Merging Between Southward IMF and the Earth's Magnetosphere	16
6. (a) Schematic Diagram of Various Observed Magnetospheric Boundary Layers; (b) Their Mapping Down to the Ionosphere Along Magnetic Field Lines	18
7. A Model of Magnetospheric Circulation for Filling the Plasma Sheet	18
8. The Distribution of Plasma Sheet Electrons in the Equatorial Plane	21
9. The Distribution of Nightside, Plasma Sheet Electrons in the Meridional Plane	21
10. Cross-Sectional View of Magnetotail Looking Earthwards	22
11. Shapes of Last Closed Equipotential for Various Values of v	31
12. Isocontours of Distribution Functions With (a) Isotropic and (b) Loss Cone Distributions	32
13. Outline of Self-Consistent Calculation of Magnetospheric Convection	34
14. (a) Field-Aligned Currents and Electric Fields as Seen by a Polar Orbiting Satellite in the Dawn-Dusk Meridian	37
14. (b) Idealized Electric Field and Magnetic Perturbation Measurements	39
15. Two Examples of Large-Scale Electric Fields Measured by OGO-6	41
16. Types of Electric Field Patterns Observed by OGO-6, and Their Dependence on the Interplanetary Magnetic Field B_X and B_Y	42
17. Scatter Plot of Convective Electric Field Patterns Observed By S3-2 as a Function of IMF B_X and B_Y	43
18. Example of Sunward Convection and a Dusk-to-Dawn Electric Field in the Central Polar Cap During a Period of Northern IMF	44
19. Cross-Polar-Cap Potential as a Function of Solar Wind Parameter ϵ	46
20. Typical Differential Spectra for the Polar Rain and Cleft Precipitation Observed on Orbit 1176 on 15 May 1969	47

Illustrations (contd)

21. Differential Electron Energy Spectra Measured in the Polar Cap, The Tail Lobe, and the Magnetosheath (Dashed Curves)	49
22. Cartoon Representation of Sequential DMSP High-Latitude Imagery on 12 December 1977	51
23. The Dawn-to-Dusk Electric Field Component and the Transverse Magnetic Field Deflection (Top Panel), and the Directional Electron Flux and Pitch Angles (Bottom Panel)	52
24. Idealized Two-Dimensional Projection of Electric Fields and Currents in the Vicinity of Event 6 in Figure 23	53
25. A Summary of the Distribution and Flow Directions of Large-Scale, Field-Aligned Currents Determined From (a) Data Obtained From 439 Passes of Triad During Weakly Disturbed Conditions, and (b) Data Obtained From 366 Triad Passes During Active Periods	55
26. Volland-Stern Injection Boundaries for $v = 2$ and $v = 3$, Rotated to Fit the Inner Edge of the Plasma Sheet as Determined by the DMSP/F2 Auroral Boundaries, for Various K_p	58
27. Equatorial Magnetopause With Distances Along Axes of Symmetry for Various Values of K_p	61
28. Polar Cap Potential From Heppner, and From Eq. (12) With $\varphi_0 = 0$ and φ_0 With Empirical Values	62
29. Spatial Occurrence Map of 280 Inverted-V Events	63
30. Spectrogram Displaying the Flux Ratios at 7° and 60° of an Inverted-V Event	64
31. An Example of a Rapid Electric Field Reversal Observed at 8000 km by S3-3	65
32. Schematic Diagram to Illustrate the Development of the Auroral Substorm	67

Tables

1. Satellites Capable of Measuring Electric Fields	40
2. Regression Coefficients for Auroral Boundaries in the Morning Sector	57
3. Regression Coefficients for Auroral Boundaries in the Evening Sector	57
4. The Intercepts, Slopes, Correlation Coefficients, and Sample Sizes for the Linear Regression of the Boundary Location With $V B_z$ in Each Magnetic Local Time Zone With a 1h Delay in the Value of the Interplanetary Magnetic Field Used	59

Magnetospheric and High-Latitude Ionospheric Electrodynamics

1. INTRODUCTION

This report deals with the volume of space that is bounded externally by the magnetopause, and internally by the plasmapause and the high-latitude ionosphere at an altitude of 300 km. The magnetopause separates regions of space dominated by the earth's magnetic field (magnetosphere), and by the shocked solar wind (magnetosheath). Earthward of the plasmapause, dynamics are generally controlled by corotation rather than by solar-wind driven convection. The arbitrarily chosen, low-altitude boundary in the ionosphere represents a transition below which the effects of the earth's neutral atmosphere are dominant. From the viewpoints of both cause and effect, the report is something less than self-contained. Without the geomagnetic field and the solar wind, there would be no magnetosphere and no magnetospheric electrodynamics; without solar irradiance, there would be much less of an ionosphere. Without magnetospheric electrodynamics, there would be no aurora, no high-latitude currents, no ring current, and no problems with spacecraft charging.

The term "electrodynamics" encompasses a complex of processes by which charged particles move about in the magnetosphere-ionosphere system. The nature of the processes varies from region to region within the system. Magnetic

Received for publication 12 April 1982

merging at the magnetopause, and field-aligned potential drops above the auroral ionosphere, are examples of localized electrodynamic processes. They are unified as electrodynamic processes in that they emerge, with appropriate boundary conditions, as solutions of the Vlasov-Maxwell equations. General solutions of the Vlasov-Maxwell equations over the entire magnetosphere-ionosphere system are well beyond present capabilities. Some success, however, has been achieved by considering elements of the system in relative isolation. This provides insight into how system elements evolve in response to external inputs. Since the entire system is electrically coupled, the isolated element approach is self-limiting. As one element evolves, it affects processes in other elements of the system. The main goals of this report are to describe the various system elements and indicate, in a qualitative sense, how they are electrically coupled.

In dealing with the earth's magnetosphere, three things quickly impress the mind. First, there is almost nothing there. Particle densities in the plasma sheet range up to about $1/\text{cm}^3$. With present technology, laboratory vacuum systems are able to get down to densities of $10^{10}/\text{cm}^3$. Second, the volume of space occupied by the magnetosphere is considerable. Typical magnetospheric dimensions are of the order of $10 R_E$ ($1 R_E = 6.4 \times 10^3 \text{ km}$). Third, when compressed to global scales, the effects of magnetospheric processes are impressive. This third point is illustrated in Figure 1, and provides a convenient point of departure for this survey of magnetospheric and high-latitude ionospheric processes. The figure exemplifies the spatial distribution of visible radiation observed by an optical imaging system on a DMSP (Defense Meteorological Satellite Program) satellite. City lights provide an easily recognized map of the western half of North America. The total energy emitted by auroral forms over the northern tier of Canadian provinces rivals or exceeds the combined ground emissions from the United States and Canada. Auroral emissions are largely due to plasma sheet electrons, with energies of a few keV impacting the E-layer of the ionosphere. The instantaneous locus of plasma sheet electron precipitation is called the auroral oval. Global imagery from satellites such as DMSP have shown that the auroral oval may be approximated by circular bands surrounding the geomagnetic poles. The centers of the circles are offset by about 3° to the night sides of the magnetic poles. The radii of the circle, the widths of the bands, and the intensity of emissions vary with the level of geomagnetic activity. However, the auroral oval exists at all times, and acts as a major sink for magnetospheric particles and energy. The particles and energy lost by the magnetosphere due to auroral precipitation ultimately come from the solar wind. Thus, an estimate of global precipitation loss also gives an estimate of the efficiency of solar wind/magnetospheric interactions required to maintain the auroras.



Figure 1. DMSP Imagery From Over Western North America

During periods of moderate geomagnetic activity, the auroral oval can be approximated as a circular band extending from 75° to 65° magnetic latitude. The area of such a band is 10^{17} cm^2 . The mean flux of electrons into the auroral oval is about $10^9 / \text{cm}^2\text{-sec}$. Thus, under steady state conditions, the solar wind must supply electrons to the magnetosphere at a rate of $10^{26} / \text{sec}$. The average energy of precipitating electrons is of the order of 1 keV. The energy loss due to electron precipitation alone is about 10^{10} W . Similar or larger amounts of solar wind energy must be supplied to account for ionospheric Joule heating, and for maintaining the ring current. The central focus of this report is to outline the present understanding of how 10^{26} electrons per second and tens of billions of watts are extracted from the solar wind to drive magnetospheric and ionospheric electrodynamic processes.

2. MAGNETOSPHERIC BOUNDARY INTERACTIONS

In describing interactions between the solar wind and the earth's magnetosphere, two coordinate systems are useful: geocentric solar-ecliptic (SE) and solar magnetospheric (SM) coordinates. Both coordinate systems have their origins at the center of the earth with the X axes positive toward the center of the sun; that is, $X_{SE} = X_{SM}$. The Z_{SE} axis is normal to the ecliptic plane, and positive toward the north. The Y_{SE} that completes the right-hand system is positive toward local dusk. The Z_{SM} axis is coplanar with the earth's magnetic moment vector (\vec{M}) and the X_{SM} axis. It is positive toward ecliptic north. The Y_{SM} axis, which always lies in the SM equatorial plane, completes the right-hand orthogonal coordinate system. For a radially flowing solar wind ($\vec{V}_s = -V_s \hat{X}_{SE} = -V_s \hat{X}_{SM}$, where \hat{X}_{SE} and \hat{X}_{SM} are unit vectors along X_{SE} and X_{SM} , respectively) the angle between \vec{M} and Z_{SM} gives the magnetic latitude of the magnetospheric subsolar point. Note that due to the 11° offset between \vec{M} and the earth's rotational axis, and to the 23.5° angle between the equatorial and ecliptic planes, the magnetic latitude of the subsolar point is subject to $\pm 34.5^\circ$ combined seasonal and diurnal variations. The SM is superior to the SE system for ordering data relevant to interactions between the solar wind and the magnetosphere.

2.1 The Magnetopause

The shape of the "steady state" magnetosphere is determined from the force balance equation

$$\nabla \cdot [\underline{P} + \underline{T}] = 0 \quad (1)$$

where \underline{P} and \underline{T} are the total pressure, and the Maxwell stress tensors, respectively. The total-pressure tensor is made up of two parts, due to the dynamic and thermal pressures of the solar-wind components.

$$\underline{P} = 2n_s m_p \vec{V}_s \vec{V}_s + p_{si} + p_{se} \quad (2)$$

where n_s is the solar-wind density, m_p the mass of a proton; p_{si} and p_{se} are the thermal pressures of solar-wind ions and electrons, respectively. The factor of 2 accounts for specular reflection of incoming particles. The shape of the magnetopause on the dayside can be calculated by numerical means using a simplified force balance

$$2n_s m_p V_s^2 (-\hat{X}_{SE} \cdot \hat{n}_M)^2 = B_T^2 / 2 \mu_0 \quad (3)$$

where μ_0 is the permittivity of free space, \hat{n}_M is an outward-directed unit vector, normal to the magnetopause, and \vec{B}_T is the total magnetic field at the magnetopause. \vec{B}_T is a superposition of fields due to the earth's dipole \vec{B}_D , to the currents flowing on the magnetopause \vec{B}_M , and to other currents distributed in the magnetosphere. Beyond the magnetopause, \vec{B}_M exactly cancels the internal fields. To a very good approximation at the subsolar point of the magnetopause

$$|\vec{B}_T| = 2|\hat{n}_M \times \vec{B}_D| \quad (4)$$

In the magnetic equatorial plane

$$\vec{B}_D = B_0 / L^3 \quad (5)$$

where $B_0 = 3.1 \times 10^{-5} \text{ T}$ is the strength of the earth's field at the surface on the magnetic equator. L is the distance from the center of the earth in earth radii (R_E). Substitution of Eqs. (4) and (5) into Eq. (3) gives the distance to the magnetopause near the subsolar point

$$L_M = (B_0^2 / \mu_0 n_s m_p V_s^2)^{1/6} \quad (6)$$

For a solar-wind density and velocity of $5/\text{cm}^3$ and 400 km/sec , $L_M = 9$. The shape of the dayside magnetopause was calculated by Mead and Beard,¹ and by Olson,² using iterative numerical techniques in which the tilt of the dipole was ignored and included, respectively. Figure 2 shows a meridional cross section of the magnetosphere calculated with $L_M = 10$ in the Mead and Beard model. The locus of dipole field lines (dashed lines), in comparison with the calculated total field, strikingly illustrates the effects of the solar wind on the overall magnetic topology. Magnetic field lines on the dayside are compressed, while those on the nightside are elongated. Note that in this model field lines intersecting the earth at magnetic latitudes greater than 83° are swept back to the nightside by the solar wind. There are a pair of singular points on the magnetopause at separatrices between field lines closing on the day and night sides. These points correspond to the dayside cusps.

1. Mead, G. D., and Beard, D. B. (1964) Shape of the geometric field solar wind boundary, J. Geophys. Res. 69:1169.

2. Olson, W. P. (1969) The shape of the tilted magnetopause, J. Geophys. Res. 74:5642.

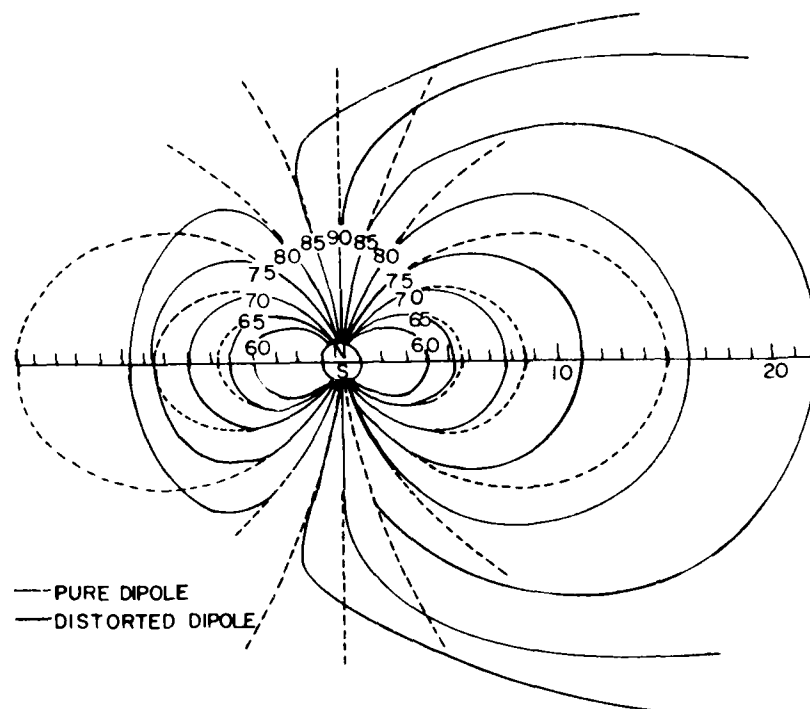


Figure 2. Model of the Earth's Magnetic Field Distorted by the Solar Wind¹

The models just discussed do not describe the nightside of the magnetotail adequately. One reason is apparent from a consideration of Eq. (2). On the day-side of the magnetosphere, the dynamic pressure of the solar wind dominates over the thermal pressures. On the nightside, with plasma flow almost tangential to the magnetopause ($\vec{V}_s \cdot \hat{n}_V \approx 0$), the converse is true. An early model³ of the magnetosphere had a teardrop shape, with the closing distance determined by the solar-wind Mach number. Piddington⁴ suggested that, in flowing past the magnetosphere, the solar wind exerts tangential stresses at the boundary. Such stresses draw the nightside of the magnetosphere into an elongated magnetotail. In the absence of significant plasma within the magnetotail, the tangential force exerted by the solar wind on the magnetosphere is

3. Johnson, F. S. (1969) The gross character of the geomagnetic field in the solar wind, *J. Geophys. Res.* 65:3049.

4. Piddington, J. H. (1963) Theories of the geomagnetic storm main phase, *Planet. Space Sci.* 11: 1277.

$$F_T = \frac{B_{MT}^2}{2\mu_0} - R_{MT}^2 \quad (7)$$

where B_{MT} and R_{MT} are the field strength and radius of the magnetotail, respectively. There are, however, distributed currents in the inner magnetosphere (the ring current), and in the magnetotail (the neutral sheet currents), whose effects must be included in realistic stress calculations.

2.2 Convection

In many cases, the magnetosphere-solar wind interaction is well described by steady state equations such as Eq. (1). The equilibrium represented by these equations, however, is dynamic rather than static. Only a dynamic situation is consistent with existing high-latitude current systems. These currents result from ionospheric convection, which is driven by magnetospheric convection.⁵ Magnetospheric convection is, in turn, driven by the solar wind. That is, energy is extracted from the solar wind by the magnetosphere, and at least some of that energy is dissipated in the ionosphere. Two mechanisms for transferring energy to the magnetosphere have been developed over the last two decades: viscous interaction⁶ and magnetic merging.⁷ Both models explain many qualitative features of magnetospheric convection and auroral particle energization. Recent satellite observations suggest that both mechanisms are operative, but in more complex ways than envisaged by early proponents.

The Oxford-Hines model⁶ postulates that the magnetosheath plasma exerts a viscous force on a layer of unspecified thickness inside the magnetopause. Magnetic field lines threading this layer are dragged in the antisolar direction, and are stretched to great distances in the magnetotail. As elongated flux tubes move out of the viscous interaction layer, they snap back to a more dipolar configuration. In the rest frame of the earth, this motion of magnetic field lines appears as an electric field, $\vec{E} = -\vec{V} \times \vec{B}$. A magnetospheric equatorial projection of the convection pattern generated in the viscous interaction model is given in Figure 3. When mapped to ionospheric altitudes, assuming that $\vec{E} \cdot \vec{B} = 0$, the model reproduces the general features of the polar/auroral current system. Note that plasma trapped on

5. Gold, T. (1959) Motions in the magnetosphere of the earth, J. Geophys. Res. 64:1219.

6. Oxford, W. I., and Hines, C. O. (1961) A unifying theory of high-latitude geophysical phenomena and geomagnetic storms, Can. J. Phys. 39:1133.

7. Dungey, J. W. (1961) Interplanetary magnetic field and the auroral zones, Phys. Rev. Lett. 6:47.

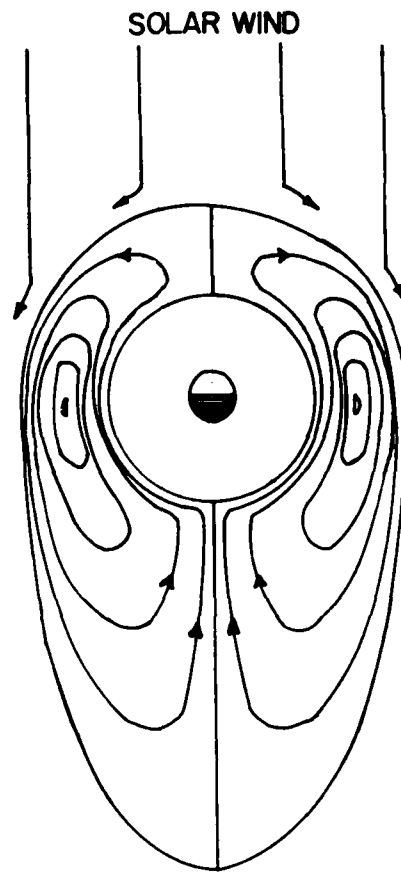


Figure 3. Equatorial Projection of Convection Pattern in Viscous Interaction Model

elongated flux tubes is adiabatically heated as the flux tubes convect earthward and shrink in volume.

The second model postulates that the dynamic interaction between the solar wind and the magnetosphere proceeds by means of a magnetic merging process. The simplest features of this phenomenon are illustrated in Figure 4. Consider a magnetic field that at great distances above (below) the X-Y plane points in the + (-) X direction. In the presence of an electric field E_Y , magnetic field lines convect toward the X-Y plane. At the neutral line ($X = 0, Z = 0$), magnetic field lines from the upper half space merge with field lines of the opposite polarity from the lower half space. To the left (right) of the neutral line, merged magnetic field lines cross the X-Y plane with a + (-) Z component, and $\vec{E} \times \vec{B}$ convect away from the neutral line in the + (-) direction. Two necessary conditions for magnetic

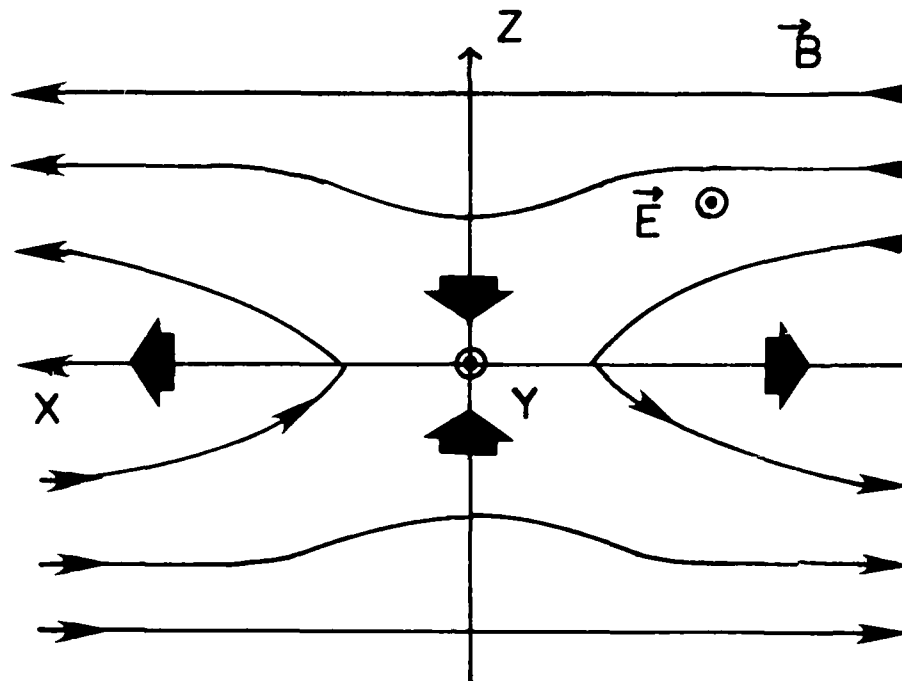


Figure 4. Magnetic Field Geometry and Electric Field Required for Magnetic Merging

merging are magnetic fields of opposite polarity across some plane, and an electric field component that is tangent to the plane.

Before considering how magnetic merging might apply to the magnetosphere, it is useful to distinguish between several possible magnetic topologies. It is well known that a weak interplanetary magnetic field (IMF) is carried by the solar wind. Except for a small correction term in the force balance equation, the IMF plays no obvious role in the viscous interaction model. The magnetic merging model, however, assigns important roles to the IMF because this model requires three types of magnetic field lines: (1) IMF lines with both "feet" in the interplanetary medium, (2) closed field lines with both "feet" in the earth, and (3) open field lines with one "foot" on earth and the other in the solar wind. Dungey⁷ pointed out that when the IMF has a southward component, magnetic merging can occur near the subsolar point of the magnetopause. The idea is illustrated in Figure 5, which can be viewed either as a snapshot, or as a time history of an individual field line. As southward directed IMF lines are convected up against compressed dipolar field lines, merging occurs at time (1). Because one foot of a newly merged field line is embedded in the solar wind, the whole field line is dragged in the antisolar ($-X_{SM}$) direction. In an earth-stationary frame of reference, the motion of the ionospheric foot of the field line appears to result from a dawn-to-dusk electric field. Times (2) through (5) show the various stages of antisunward motion of an open field line. At time (6), a

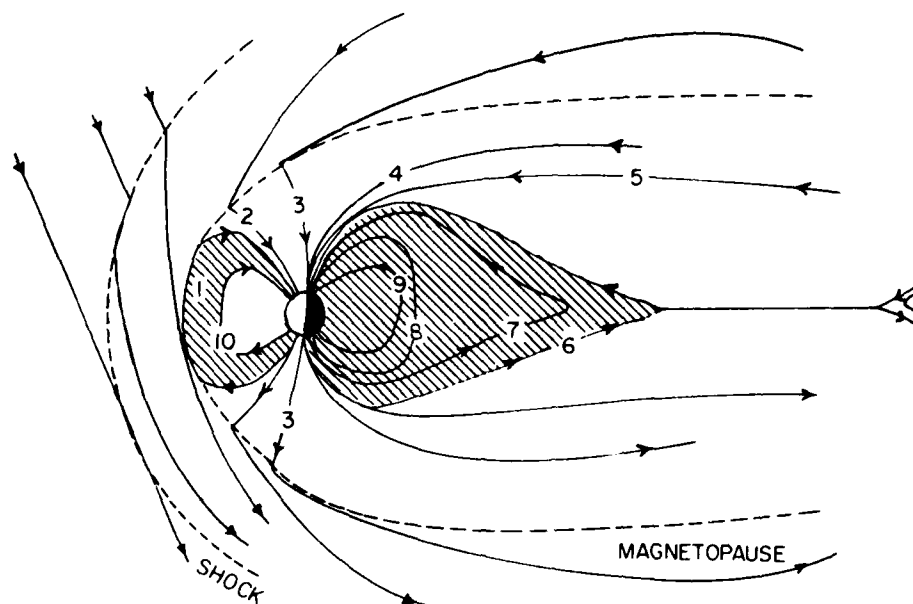


Figure 5. Snapshot of Magnetic Merging Between Southward IMF and the Earth's Magnetosphere

portion of the field line has convected to the magnetic equatorial plane where it reconnects with an open field line from the conjugate ionosphere. Under the influence of the dawn-to-dusk electric field the field line then convects earthward (times ⑦ through ⑨). Eventually, reconnected field lines move to the dayside (time ⑩), where they are in position to continue the merging-reconnection cycle.

The magnetospheric convection patterns predicted by the viscous interaction and magnetic merging models with a southward IMF are quite similar. Empirical evidence from near the magnetopause⁸⁻¹⁰ indicates that both viscous and magnetic merging processes occur. That many observational studies have shown high correlations between southward turnings of the IMF and the onset of magnetic activity

8. Eastman, T. E., Hones, Jr., E. W., Bame, S. J., and Asbridge, J. R. (1976) The magnetospheric boundary layer: site of plasma momentum and energy transfer from the magnetosheath into the magnetosphere, Geophys. Res. Lett. 3:685.
9. Russell, C. T., and Elphic, R. C. (1979) ISEE observations of flux transfer events at the dayside magnetopause, Geophys. Res. Lett. 6:33.
10. Mozer, F. S., Torbert, R. B., Fahleson, U. V., Falthammer, C. G., Gonfalone, A., Pedersen, A., and Russell, C. T. (1979) Direct observation of a tangential electric field component at the magnetopause, Geophys. Res. Lett. 6:305.

indicates a dominant role for energy transfer by a merging process. As discussed in Sec. 6.1, this surmise is supported by modifications observed in polar-cap (open field line) convection patterns, with variations in the V_{SM} component of the IMF and when the Z_{SM} component is northward. Finally, we mention that, currently, merging is thought to occur sporadically, rather than as a steady state process,¹¹ and in the vicinity of the dayside cusps rather than near the subsolar point.^{12, 13}

2.3 Boundary Layers

Before considering the dynamics of the closed portion of the magnetosphere, let us return briefly to our original question of how 10^{26} particles/sec gain entry to the plasma sheet. Between 10^{28} and 10^{29} solar wind particles/sec impact the dayside magnetopause. Thus, an entry efficiency of less than 1 percent is sufficient to maintain the plasma sheet. Our understanding of how magnetosheath plasma gains entry to the magnetosphere and influences its interior dynamics has been evolving rapidly over the last decade. Under such circumstances, it is not unusual to encounter a multiplicity of nomenclatures that will probably be simplified as relationships between various boundary plasma regimes become more evident. Vasyliunas¹⁴ has defined magnetospheric boundary layers as regions of space threaded by magnetic field lines of the magnetosphere, but populated by plasma similar to that found in the magnetosheath. The four regions satisfying this definition are: (1) the plasma mantle, (2) the interior cusp, (3) the low-latitude boundary layer, and (4) the plasma sheet boundary layer. Figure 6 is a schematic representation of the magnetospheric loci of these regimes. Somewhat speculative representations of their ionospheric projections, and their "source-relationships" to the plasma sheet, are given in Figures 6b and 7, respectively. The plasma mantle is found on open magnetic field lines; the remaining three regions are found in closed field line portions of the magnetosphere.

-
11. Haerendel, G., Paschmann, G., Sekopke, N., Rosenbauer, H., and Hedgecock, P. C. (1978) The frontside boundary layer of the magnetosphere and the problem of reconnection, J. Geophys. Res. 83:3195.
 12. Crooker, N. U. (1977) Dayside merging and cusp geometry, J. Geophys. Res. 82:3629.
 13. Crooker, N. U. (1979) The magnetospheric boundary layers: a geometrically explicit model, J. Geophys. Res. 84:951.
 14. Vasyliunas, V. M. (1979) Interaction between the magnetospheric boundary layers and the ionosphere, Proc. Magnetospheric Boundary Layers Conf. (ESA SP-148) Alpbach, Austria, p. 337.

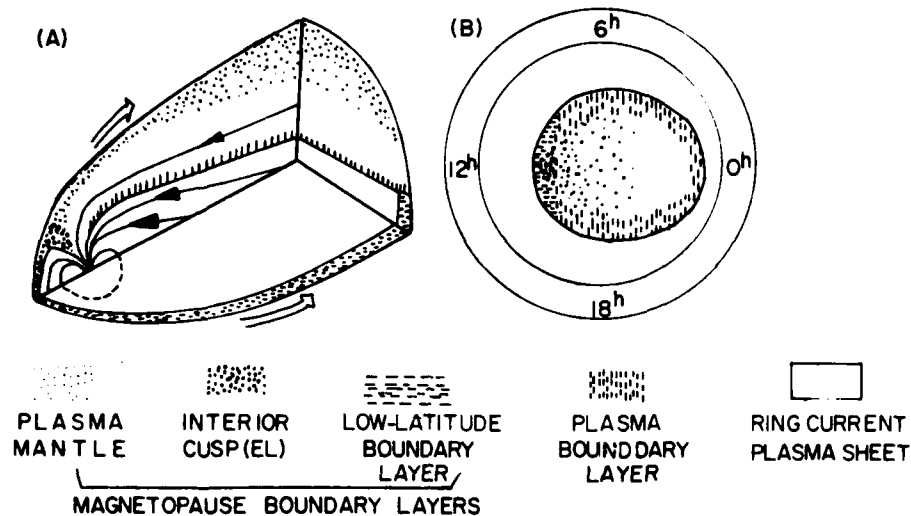


Figure 6. (a) Schematic Diagram of Various Observed Magnetospheric Boundary Layers; (b) Their Mapping Down to the Ionosphere Along Magnetic Field Lines¹⁴

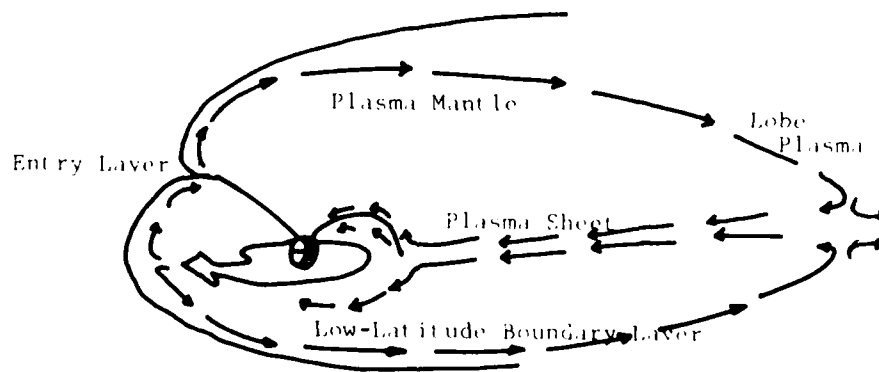


Figure 7. A Model of Magnetospheric Circulation for Filling the Plasma Sheet¹⁵

15. Freeman, J. W. (1979) Internal magnetospheric plasma flow, Proc. Magnetospheric Boundary Layers Conf. (ESA SP-148) Alpbach, Austria, p. 351.

The plasma mantle was identified first as a magnetosheath-like plasma flowing nearly along magnetic field lines inside the magnetopause, in the near-earth lobes of the magnetotail.¹⁶ The plasma density and the spatial thickness of the mantle are greatest during periods of southward IMF.¹⁷ The mantle is also observed in the lobes of the magnetotail at lunar distances ($X_{SM} = -60 R_E$) near the ecliptic plane.¹⁸ Mantle particles are believed to enter the magnetosphere near the dayside cusp. A dawn-to-dusk electric field causes particles to convect in the antisunward direction, so that particles that mirror at low altitudes find themselves on open field lines as they rise from their mirror points. The same dawn-to-dusk electric field causes the mantle particles to drift toward the equatorial plane as they move away from the earth. Pilipp and Morfill¹⁹ suggested that mantle particles may be one source of plasma sheet particles.

As the name suggests, the "interior cusp" refers to the region of closed magnetic field lines passing through or just equatorward of the cusp. Magnetosheath plasma diffuses into this region. As opposed to the mantle or the low-latitude boundary layer, the plasma of this region, which is also called the entry layer, is relatively stagnant. However, depending on the strength and direction of convective electric fields in the cusp, it is possible to think of the interior cusp plasma as a partial source of both the mantle and the low-latitude boundary layer.

Along the dawn and dusk meridians, near the magnetospheric equatorial plane, the low-latitude boundary layer is characterized by magnetosheath-like plasma flowing in the antisunward direction. The thickness of this layer ranges up to $\sim 1 R_E$. As shown in Figure 6a, the low-latitude boundary layer has been observed to great distances in the antisolar direction. The density of plasma within the layer is about a factor of 4 less than that of the adjacent magnetosheath.²⁰ Electrons within the

-
16. Rosenbauer, H., Grunwald, H., Montgomery, M. D., Paschmann, G., and Skopke, N. (1975) HEOS 2 plasma observations in the distant polar magnetosphere: the plasma mantle, J. Geophys. Res. 80:2723.
 17. Skopke, N., Paschmann, G., Rosenbauer, H., and Fairfield, D. H. (1976) Influence of the interplanetary magnetic field on the occurrence and thickness of the plasma mantle, J. Geophys. Res. 81: 2687.
 18. Hardy, D. A., Hills, H. K., and Freeman, J. W. (1975) A new plasma regime in the distant geomagnetic tail, Geophys. Res. Lett. 2:169.
 19. Pilipp, W. G., and Morfill, G. (1978) The formation of the plasma sheet resulting from plasma mantle dynamics, J. Geophys. Res. 83:5670.
 20. Skopke, N., Paschmann, G., Haerendel, G., Sonnerup, B. U. O., Bame, S. J., Forbes, T. G., Hones, Jr., E. W., and Russell, C. T. (1981) Structure of the low-latitude boundary layer, J. Geophys. Res. 86:2099.

layer have trapped pitch-angle distributions.²¹ Whether the low-latitude boundary layer is maintained through a diffusive and/or an impulsive²² entry process is currently a matter of debate. Sckopke et al.²⁰ estimate that a diffusion coefficient of $10^9 \text{ m}^2/\text{sec}$ is required to maintain the observed low-latitude boundary layer. Figure 6a shows the plasma boundary layer together with the low-latitude boundary layer as forming a continuous envelope surrounding the hot plasma contained in the central plasma sheet. The physical processes that connect the low-latitude boundary layer and/or the mantle with the plasma boundary layer, and with the central plasma sheet, are not known at this time. It is currently believed that discrete arcs in the auroral oval map to the boundary rather than to the central plasma sheet. Within the plasma sheet boundary, rapidly flowing plasmas are observed. These flowing plasmas come from spatially limited acceleration regions called "magnetospheric fireballs."²³ Whether the energization process in fireballs results from magnetic reconnection or some other process is still another open question.

3. THE PLASMA SHEET

The earth's plasma sheet is the highly dynamical region of the earth's magnetosphere that acts as a depository for auroral particles. It is a region of closed magnetic field lines. Before being detected by the Soviet satellites Luna I and Luna 2,²⁴ somewhat strangely, this important region of the magnetosphere was not anticipated theoretically. Equatorial and noon-midnight meridional projections of the plasma sheet are given in Figures 8 and 9, respectively.²⁵ Both projections

-
21. Eastman, T. E., and Hones, Jr., E. W. (1979) Characteristics of the magnetospheric boundary layer and magnetopause layer as observed by IMP 6, J. Geophys. Res. 84:2019.
 22. Lemaire, J., and Roth, M. (1978) Penetration of solar wind plasma elements into the magnetosphere, J. Atmos. Terr. Phys. 40:331.
 23. Frank, L. A., Ackerson, K. L., and Lepping, L. P. (1976) On hot tenuous plasmas, fireballs and boundary layers in the earth's magnetotail, J. Geophys. Res. 81:5859.
 24. Gringanz, K. I., Bezrukikh, V. V., Ozerov, V. D., and Rybchinskii, E. E. (1961) A study of the interplanetary ionized gas, high-energy electrons, and corpuscular radiation from the sun by means of the three-electrode trap for charged particles on the second Soviet cosmic rocket, Sov. Phys.-Dokl. 5:361.
 25. Vasyliunas, V. M. (1972) Magnetospheric Plasma, in Solar Terrestrial Physics, E. Dyer, Ed., D. Reidel Co., Dordrecht, Holland, p. 192.

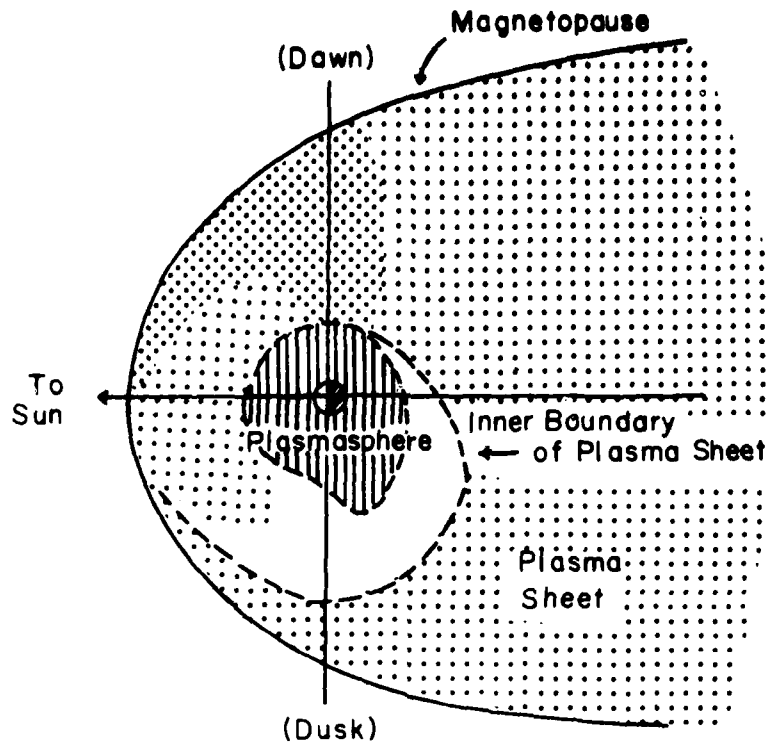


Figure 8. The Distribution of Plasma Sheet Electrons in the Equatorial Plane.²⁴
The density of shading is roughly proportional to the density of plasma sheet particles²⁵

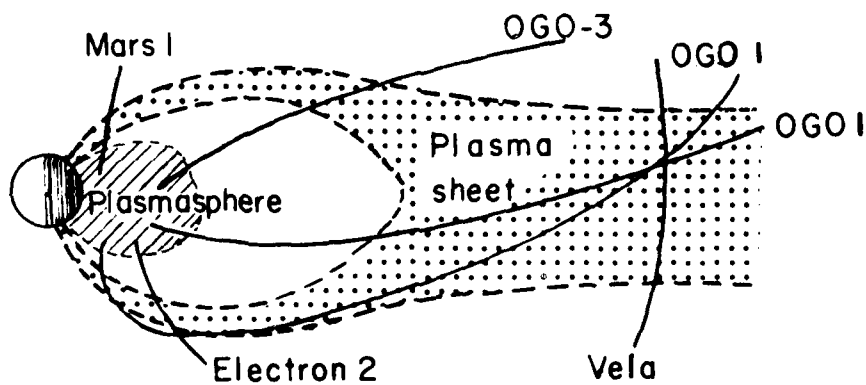


Figure 9. The Distribution of Nightside, Plasma Sheet Electrons in the Meridional Plane²⁶

show that the plasma sheet extends for great distances in the $-X_{SM}$ direction. The plasma sheet has a distinct inner edge that varies as a function of local time and the level of geomagnetic activity.^{26, 27} The dynamics of the inner edge of the plasma sheet are well understood theoretically and are discussed in Sec. 7.2. The equatorial thickness of this boundary is $\sim 1 R_E$, and is marked by a cooling of electron temperatures. Just tailward of this boundary, plasma sheet electrons have an average energy of ~ 1 keV. During periods of substorm injections, the temperature of electrons may rise to ~ 10 keV. Temperatures of plasma sheet ions tend to be higher than those of electrons by a factor of 2 or more.

Figure 10 is a cross-sectional view of the magnetotail portion of the plasma sheet. It has a minimum thickness in the mid-tail region, and flares to a maximum thickness near the dawn and dusk flanks of the tail. At lunar distance ($X_{SM} = -60 R_E$),

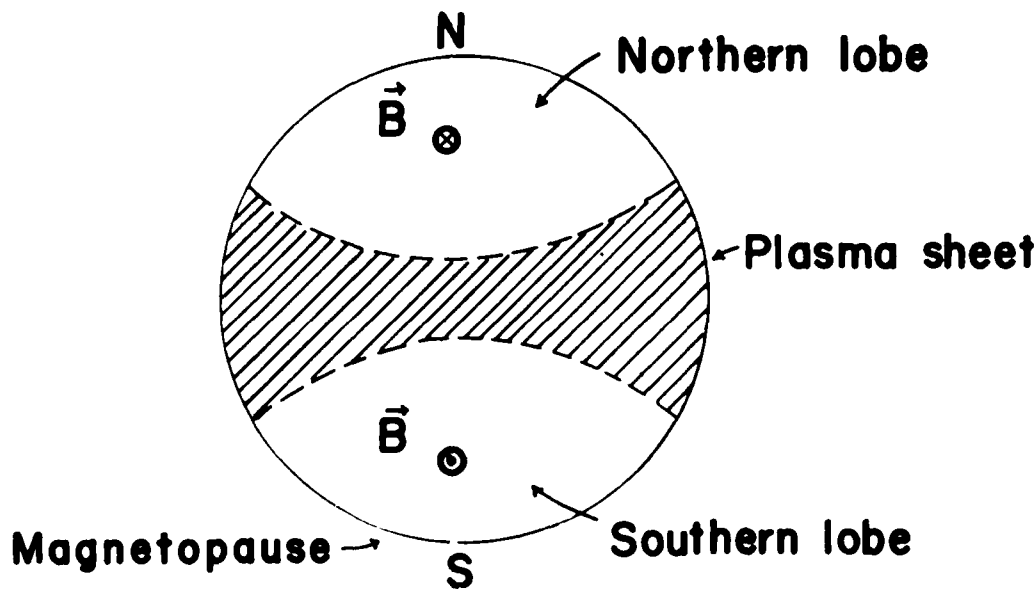


Figure 10. Cross-Sectional View of Magnetotail Looking Earthward

26. Vasyliunas, V. M. (1968) A survey of low-energy electrons in the evening sector of the magnetosphere with OGO-1 and OGO-3, *J. Geophys. Res.* 73:2839.
27. Frank, L. A. (1971) Relationship of the plasma sheet, ring current, trapping boundary, and plasmapause near the magnetic equator and local midnight, *J. Geophys. Res.* 76:2265.

the tail radius is $\sim 25 R_E$. The average half-thickness of the mid-tail plasma sheet is $\sim 3 R_E$. During the expansion phase of substorms, the thickness of the plasma sheet in the tail decreases, and then expands during the recovery phase.²⁸ At lunar distance, the average density of the plasma sheet is $\sim 0.1 \text{ cm}^{-3}$. The electron and proton temperatures are ~ 0.25 and 2.5 keV , respectively.²⁹

The remainder of this subsection is concerned with the physical mechanisms responsible for particle energization and precipitation in the plasma sheet. Energization processes are classified as either adiabatic or non-adiabatic. Examples of non-adiabatic energization are neutral sheet acceleration,³⁰ stochastic wave-particle acceleration, and heating derived from magnetic field reconnection and annihilation. Although these are undoubtedly important sources of particle energy, we limit ourselves here to describing adiabatic energization in some detail. Particle precipitation is maintained or enhanced either by magnetic field-aligned electric fields (E_{\parallel}), or by pitch-angle diffusion. E_{\parallel} is very important for discrete auroral arc formation. Pitch-angle diffusion results from wave-particle interactions. Here we summarize briefly the collective plasma modes responsible for these phenomena.

3.1 Adiabatic Motion in the Plasma Sheet

The adiabatic energization of plasma sheet particles involves the related concepts of adiabatic invariance and guiding center motion. The general concept of adiabatic invariance comes from classical Hamilton-Jacobi theory.³¹ If a system executes a periodic motion in a force field (F) that changes slowly in time with respect to the period (T)

$$\frac{1}{F} \frac{dF}{dt} \ll \frac{1}{T}$$

-
- 28. Hones, Jr., E. W., Asbridge, J. R., Bame, S. J., Montgomery, M. D., and Singer, S. (1973) Substorm variations of the magnetotail plasma sheet from $N_{SM} \approx -6 R_E$ to $N_{SM} \approx -60 R_E$, J. Geophys. Res. 78:109.
 - 29. Rich, F. J., Reasoner, D. L., and Burke, W. J. (1973) Plasma sheet at lunar distance: Characteristics and interactions with the lunar surface, J. Geophys. Res. 78:8097.
 - 30. Speiser, T. W. (1967) Particle trajectories in model current sheets, II: Application to auroras using a geomagnetic tail model, J. Geophys. Res. 72:3919.
 - 31. TerHaar, D. (1964) Elements of Hamiltonian Mechanics, North Holland Co., Amsterdam, Ch. 6.

then the quantity

$$I = \oint p \, dq,$$

(where p and q are canonical momentum and coordinate variables) is a constant of the motion known as an adiabatic invariant. Charged particles moving in the earth's magnetic field may have as many as three periodicities due to their gyration, bounce, and drift motions. The three adiabatic invariants associated with these periodicities are:

- (1) the magnetic moment

$$\mu = \frac{m v_{\perp}^2}{2B} \quad (8)$$

where v_{\perp} is the component of velocity perpendicular to the magnetic field,

- (2) the longitudinal invariant

$$J = \oint p_{\parallel} \, ds \quad (9)$$

where p_{\parallel} and ds are momentum component and distance along B , and

- (3) the flux invariant

$$\Psi = \oint \vec{A} \cdot d\vec{l} \quad (10)$$

where \vec{A} is the magnetic vector potential and $d\vec{l}$ a distance element along a particle drift trajectory.^{32,33} Most plasma sheet particles either precipitate or follow drift trajectories that intersect the magnetopause before they can drift all the way around the earth. Thus, in the plasma sheet only the first and second invariants are of interest. The third invariant is important for understanding the ring current and radiation belts.

32. Northrop, T. G. (1963) The Adiabatic Motion of Charged Particles, Interscience, New York, Ch. 3.

33. Rossi, B., and Olbert, S. (1970) Introduction to the Physics of Space, McGraw-Hill, New York, Ch. 5.

At this point, it is useful to introduce the related concepts of pitch angle and magnetic mirroring. The pitch angle (α) of a charged particle is defined as the angle between its instantaneous velocity and the magnetic field

$$\alpha = \cos^{-1} (\vec{v} \cdot \vec{B} / |\vec{v}| |\vec{B}|) .$$

Magnetic mirroring results from the constancy of a particle's magnetic moment and total energy. The total energy of a non-relativistic particle of mass m and charge q moving with a velocity v in combined magnetic and electric fields is

$$\epsilon = 1/2 m v_{\parallel}^2 + \mu B + q \Phi \quad (11)$$

where Φ is the electrical potential. The component of force exerted along \vec{B} is

$$m \frac{dv_{\parallel}}{dt} = -\mu \frac{\partial B}{\partial s} - q \frac{\partial \Phi}{\partial s} . \quad (12)$$

The second term on the right-hand side of Eq. (12) is due to field-aligned electric field components that are discussed regarding auroral arc formation. The first term on the right hand side of Eq. (12) is the magnetic mirror force. A particle at the magnetic equator ($s = 0$) with pitch angle α_{eq} can move earthward along \vec{B} until its pitch angle reaches 90° ($v_{\parallel} = v \cos \alpha = 0$). At this point, it is reflected by the mirror force toward the magnetic equator. The strength of the magnetic field at the mirror point is designated B_M . The total kinetic energy of a particle at its mirror point is $1/2 m v^2 = \mu B_M$. Since, in general, $\mu = 1/2 m v^2 (\sin^2 \alpha) / B$, the magnetic mirroring condition, in the absence of E_{\parallel} , is often written

$$\sin^2 \alpha = B / B_M . \quad (13)$$

The line integration for the longitudinal invariant proceeds from the magnetic equator to the mirror distance s_M .

The notion of guiding center motion is more general than that of adiabatic motion. Under many circumstances, charged particle motions are well-approximated by superpositions of motions of guiding centers and gyration about the guiding center. For example, in a uniform magnetic field, the equation of motion

$$m \frac{d\vec{v}}{dt} = q (\vec{v} \times \vec{B}) \quad (14)$$

describes a particle that gyrates with a circular frequency $\Omega = qB/m$ about a field line, and moves along the field line (its guiding center) with a constant velocity. In the presence of an external force field \vec{F} that is perpendicular to \vec{B} , the equation of motion

$$m \frac{d\vec{v}}{dt} = q (\vec{v} \times \vec{B}) + \vec{F} \quad (15)$$

can be reduced to the form of Eq. (14) by transforming to a coordinate system moving with a drift velocity

$$\vec{v}_D = \frac{\vec{F} \times \vec{B}}{qB^2} \quad (16)$$

In this frame of reference, the motion of the particle about \vec{B} is purely gyrational.

The most important drifts within the magnetosphere are caused by electric fields.

$$\vec{v}_E = \frac{\vec{E} \times \vec{B}}{B^2} \quad (16)$$

magnetic field gradients

$$\vec{v}_G = \frac{\vec{B} \times \nabla B}{qB^2} \quad (17)$$

and magnetic field line curvature

$$\begin{aligned} \vec{v}_C &= \frac{mv^2}{R^2} \left(\frac{\vec{R} \times \vec{B}}{qB^2} \right) \\ &= mv^2 \left(\frac{\vec{B} \times (\vec{B} \cdot \nabla) \vec{B}}{qB^4} \right) \end{aligned} \quad (18)$$

where \vec{R} is the magnetic field line radius-of-curvature vector. Note that \vec{v}_G and \vec{v}_C depend on both the particle's energy and charge; \vec{v}_E depends on neither. Protons (electrons) gradient and curvature drift toward the west (east). In the nearly dipolar part of the inner plasma sheet, \vec{v}_G and \vec{v}_C are of comparable magnitudes. Due to sharp magnetic field line curvature across the neutral sheet $\vec{v}_C > \vec{v}_G$ in the magnetotail.

With the expressions for the adiabatic invariants [Eqs. (8) and (9)], and guiding center drifts [Eqs. (16), (17), and (18)], we may understand: (1) the adiabatic heating of magnetospheric plasma, (2) the existence of a ring current, and (3) the position of the inner boundary of the plasma sheet.

Both the viscous interaction and the magnetic merging models require that particles in the nightside plasma sheet be "adiabatically" heated as they convect earthward under the influence of a dawn-to-dusk electric field. In this motion, each particle's magnetic moment $1/2 m v_{\perp}^2 / B$ is a constant. Consider a particle mirroring in the equatorial plane, $J = 0$ [Eq. (9)]. As it drifts from, say, $30 R_E$ in the magnetotail where $B \sim 20$ nT, to a distance of $6 R_E$ where $B \sim 140$ nT, its kinetic energy must increase sevenfold. Particles with $J \neq 0$ gain kinetic energy, not only from the conservation of μ , but also from the apparent motion of magnetic mirror points (conservation of J). In moving from equatorial crossings of $30 R_E$ to $6 R_E$, particles find themselves on shorter and shorter field lines. Since $\oint \mathbf{p} \cdot d\mathbf{s}$ must be a constant, p_{\parallel} must increase as particles convect earthward.

From the conservation of energy, it is seen that an increase in particle kinetic energy must be due to a decrease in potential energy. The potential energy is electrical. That is,

$$\frac{1}{2} (1 - \beta^2) = q \langle \mathbf{V}_D \cdot \mathbf{E} \rangle \quad (19)$$

The brackets in Eq. (19) are used to represent time averaging over a gyroperiod, and \mathbf{V}_D is the total drift velocity. Since \mathbf{V}_E is perpendicular to \mathbf{E} , only \mathbf{V}_G and \mathbf{V}_C contribute. Hines³⁴ has shown that the energy gained by "adiabatically compressing" a magnetospheric plasma is equivalent to the kinetic energy gained by gradient and curvature drifting in the direction of an electrostatic potential gradient.

Guiding center motion is the simplest basis for understanding the earth's ring current. The existence of a westward current encircling the earth can be inferred directly from decreases in surface values of the horizontal component of the earth's field during the main and recovery phases of magnetic storms. The general expression for current density is given by a sum over plasma species

$$\mathbf{j} = \sum_{\sigma} n_{\sigma} q_{\sigma} \mathbf{V}_{D\sigma} \quad .$$

34. Hines, C. O. (1963) The energization of plasma in the magnetosphere: Hydro-magnetic and particle drift approaches, Planet. Space Sci. 10:239.

Assuming, for simplicity, that the ring current is made up of a single ion species (H^+), then the current density is

$$\vec{j}_R = nq (\vec{V}_{Di} - \vec{V}_{De}) \quad (20)$$

Since \vec{V}_E is independent of charge, only \vec{V}_G and \vec{V}_C contribute to Eq. (20). Recall that for protons (electrons), \vec{V}_G and \vec{V}_C are westwards (eastwards). In an equivalent fluid description, \vec{j}_R is driven by magnetospheric pressure gradients. During the main phases of magnetic storms and the expansion phases of substorms, particles are energized and injected into the inner magnetosphere by intense electric fields. With the onset of recovery phases, the electric fields decrease in intensity and/or are shielded from the inner magnetosphere. Injected particles find themselves on closed, stably trapped orbits in which they gradient and curvature drift around the earth. During recovery, these particles are slowly removed from the ring current by precipitation, or by charge exchange with low-energy neutrals.

The position and shape of the inner edge of the plasma sheet is determined by the drift motions of plasma sheet particles. \vec{V}_E decomposes into drifts due to "convective" (\vec{V}_{EC}) and "corotational" (\vec{V}_{EA}) electric fields. In the following discussion, we use the symbols E_C to represent the "convective" electric field imposed by the solar wind on the magnetosphere, and E_A to represent the corotation electric field. The direction of \vec{V}_{EA} is eastward for all particles. For simplicity, let us consider the drift motions of charged particles having pitch angles in the equatorial plane of 90° . Conservation of energy [Eq. (11)] immediately tells us that cold ($\alpha = 0$) particles are constrained to $\vec{E} \times \vec{B}$ drift along equipotentials. Particles with non-zero α drift along surfaces of constant $(q\phi + \mu B)$.

In the magnetotail, particles predominantly drift earthward under the influence of a dawn-to-dusk E field. As they approach the earth, electrons acquire significant eastward drifts due to both \vec{V}_G and \vec{V}_{EA} . Since both of these drifts are eastward, cold electrons, with $\vec{V}_G = 0$, drift closer to the earth before their eastward drifts dominate over their earthward drifts. For this reason, outbound satellites encounter cold electrons before hot electrons at the plasma sheet's inner edge.³⁵

The boundary between cold electrons that drift along equipotentials from the tail and those that corotate on closed trajectories is called the zero energy Alfvén layer, or the inner boundary of the plasma sheet. Under steady convective electric field conditions, cold electrons that drift in from the magnetotail, without

35. Kivelson, M. G., Enge, S. M., and Southwood, D. J. (1979) The physics of plasma injection events, in Dynamics of the Magnetosphere, S. -I. Akasofu, Ed., D. Reidel Co., Hingham, Massachusetts, p. 395.

precipitating, eventually cross the dayside magnetopause. Thus, the inner boundary of the plasma sheet is the boundary between closed (corotation dominated) and open (convection dominated) equipotentials.

Before calculating the shape of the last closed equipotential, we note that for protons, \vec{V}_C and \vec{V}_{E_C} are oppositely directed. This leads to more complex drift paths for protons than electrons. Protons with $u \neq 0$ can drift earthward of the zero-energy Alfvén boundary in the evening local time sector. The different drift paths of protons and electrons eventually lead to the buildup of polarization electric fields near the inner edge of the plasma sheet. The main effects of the polarization field are to shield \vec{E}_C from the inner magnetosphere, and to distort its dawn-to-dusk orientation in the plasma sheet.

As a function of distance R , and local time φ , in the equatorial plane of the magnetosphere, the form of the electric potential is

$$\Phi(R, \varphi) = \frac{-\Omega B_0 R^3}{R} + C R^\gamma \sin \varphi \quad (21)$$

where $\Omega = 7.3 \times 10^{-5} \text{ sec}^{-1}$ is the angular spin velocity of the earth, C is a constant to be determined, and γ is a parameter that reflects the level of electrical shielding. The case $\gamma = 1$ corresponds to a uniform, dawn-to-dusk \vec{E}_C that completely penetrates the inner magnetosphere. Best empirical values of γ are in the range of 2 to 3.^{36,37} The value of C is determined by noting that \vec{E}_C is directed radially inward, and \vec{E}_A is mostly in the Y_{SM} direction. In the dusk sector, \vec{E}_C and \vec{E}_A are oppositely directed. Depending on the strength of \vec{E}_C , there is a stagnation point along the 1800 LT ($\varphi = 3\pi/2$) axis of symmetry where the two fields exactly cancel,

$$\left. \frac{\partial \Phi(R, \frac{3\pi}{2})}{\partial R} \right|_{R=R_S} = 0 \quad (22)$$

Substitution of Eq. (21) into Eq. (22) gives

$$C = \frac{\Omega B_0 R_S^3}{\gamma R_S^{(\gamma+1)}} \quad (23)$$

36. Ejiri, M., Hoffman, R. A., and Smith, P. H. (1978) The convection electric field model for the magnetosphere based on Explorer 45 observations, J. Geophys. Res. 83:4811.
37. Gussenhoven, M. S., Hardy, D. A., and Burke, W. J. (1981) DMSP/F2 electron observations of equatorward auroral boundaries and their relationship to magnetospheric electric fields, J. Geophys. Res. 86:768.

Thus,

$$\Phi(L, \phi) = -\frac{\Omega B_0 R_E^2}{L_S} \left[\left(\frac{L_S}{L} \right) - v \left(\frac{L}{L_S} \right)^v \sin \phi \right] \quad (24)$$

where we have made the substitution $L = R/R_E$ and $L_S = R_S/R_E$. The common term $\Omega B_0 R_E^2$ is ~ 90 kV. The potential of the stagnation point is

$$\Phi(L_S, \frac{3\pi}{2}) = -\frac{90}{L_S} [1 + 1/v] \text{ kV} \quad (25)$$

Since along the $\phi = 3\pi/2$ line $E_C < (>) E_\infty$ for $L < (>) L_S$, Eq. (25) gives the potential of the zero-energy Alfvén boundary. By setting the term in brackets on the right-hand side of Eq. (24) equal to $[1 + 1/v]$, we arrive at the equation for the zero-energy Alfvén boundary in the equatorial plane as a function of distance from the center of the earth (L_A) and local time

$$\left(\frac{L_A}{L_S} \right)^{v+1} \sin \tau + (v+1) \frac{L_A}{L_S} - v = 0 \quad (26)$$

Southwood and Kaye³⁸ have shown that to an excellent approximation

$$L_A = L_S / (1 + \frac{2S}{v}) \quad (27)$$

where $S = \left| \cos \frac{\tau - \tau/2}{2} \right|$. The solution is exact when $v = 1$. Figure 11 shows that the shape of the last equipotential varies from an elongated teardrop for $v = 1$, to a circle for $v = \infty$. Note that Eqs. (26) or (27) only allow calculations of the shape, but not the distance to the Alfvén boundary. L_S depends on E_C , which varies with conditions in the solar wind, and with the level of magnetic activity. It is convenient to defer further comment on the Alfvén boundary until we have discussed its ionospheric projection, the equatorward boundary of diffuse auroral precipitation.

3.2 Pitch Angle Diffusion of Plasma Sheet Particles

The final topic to be considered under the heading of general magnetospheric processes is particle precipitation. To anticipate our discussion of the ionosphere,

38. Southwood, D. J., and Kaye, S. M. (1979) Drift boundary approximations in simple magnetospheric convection models, J. Geophys. Res. 84:5773.

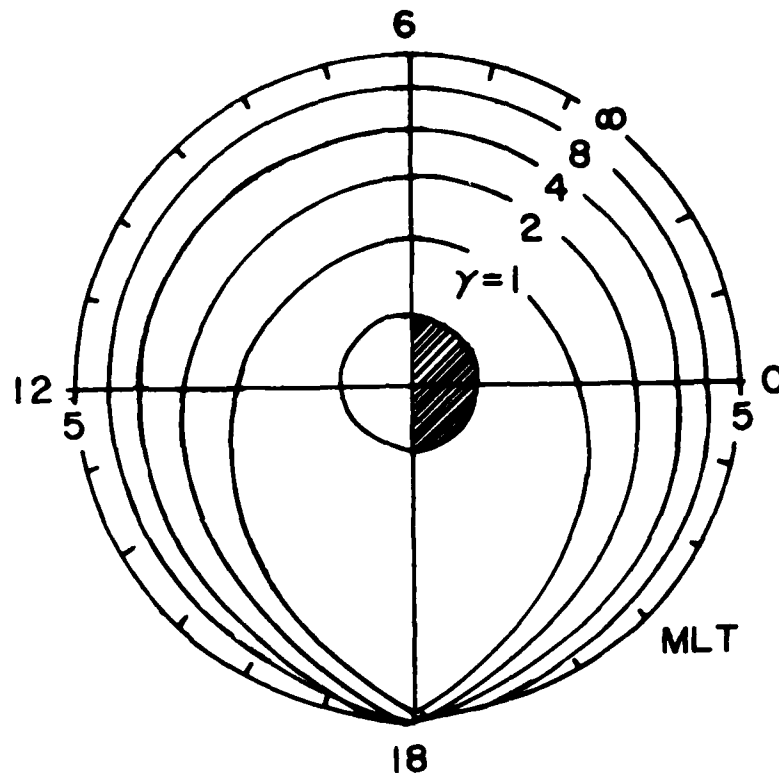


Figure 11. Shapes of Last Closed Equipotential for Various Values of v^{36}

we note that instrumentation on satellites passing through the diffuse auroral ionosphere measures fluxes of electrons and protons that are isotropic over the down-coming hemisphere. The continuous precipitation of plasma sheet electrons and protons into the auroral ionosphere cannot be explained in terms of the individual particle model that we have been using. The problem is illustrated simply in Figure 12, where we sketch sequential isocontours of particle distribution functions in the magnetospheric equatorial plane. Figure 12a represents an isotropic population at some initial time. Particles with $\alpha_{eq} \neq 90^\circ$ ($v \neq 0$) move along field lines toward their mirror points. If their mirror points are sufficiently deep in the atmosphere, typically altitudes < 200 km, the particles are lost. Otherwise they return to the magnetosphere. If we designate the strength of the magnetic field at

an altitude of 200 km as $B(200)$, then Eq. (13) shows that particles initially with equatorial pitch angles

$$\alpha_{eq} = \alpha_{L_0} = \sin^{-1} \left[\frac{B_{eq}}{B(200)} \right]^{-1/2} \quad (28)$$

are lost after a few bounce periods. Such particles are said to be in the atmospheric loss cone. For plasma sheet particles, α_{L_0} is $\sim 2^\circ$. Figure 12b shows the distribution after several bounce periods as made up of the initial population minus an empty loss cone. Particle motion that conserves μ and J allows no further loss.

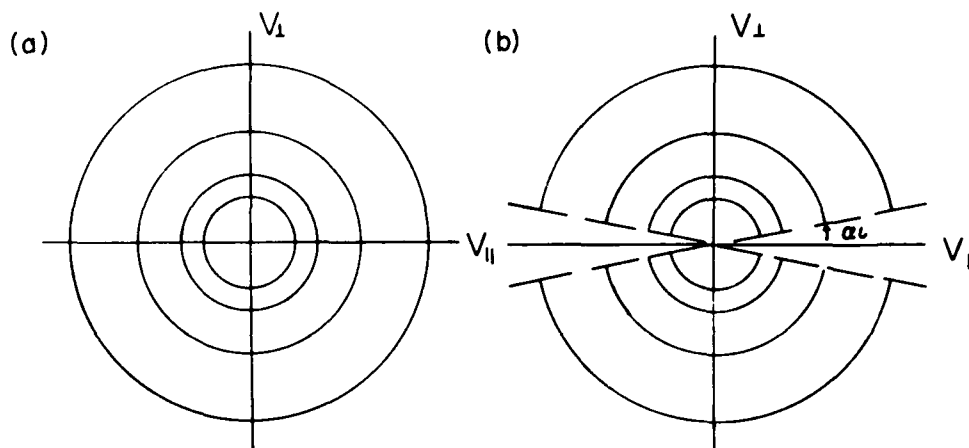


Figure 12. Isocontours of Distribution Functions With (a) Isotropic and (b) Loss Cone Distributions

Kennel and Petschek³⁹ pointed out that above certain particle flux levels, loss cone distribution functions such as shown in Figure 12b are unstable to the growth of whistler waves. The waves grow in energy by causing particles to diffuse into the loss cone. To produce strong pitch-angle diffusion, that is, maintain isotropy over the loss cone, a resonant condition must be fulfilled. Resonant scattering occurs for particles whose energy is equal to that of the magnetic energy per particle

$$\text{Res} = \frac{B^2}{2 \mu_0 n} \quad (29)$$

39. Kennel, C. F., and Petschek, H. E. (1966) Limit on stably trapped particle fluxes, J. Geophys. Res. 71:1.

This model successfully explains flux limits observed for stably trapped ring current particles. The requirement for resonant pitch-angle diffusion given in Eq. (29) was empirically verified by observations of the proton ring current from Explorer 45 during the magnetic storm of December 1971.⁴⁰

An examination of the resonance condition given in Eq. (29) shows that a whistler mode instability cannot be responsible for strong pitch-angle scattering in the plasma sheet. At geostationary altitude ($6.7 R_E$) in the plasma sheet, $B \sim 100$ nT and $n \sim 1/\text{cm}^3$. This gives a magnetic field energy density in eV/cm^3 of $2.5 B^2 (\text{nT})$. A resonant energy of ~ 25 keV is well in excess of mean thermal energies for either electrons or protons in the plasma sheet.

Realizing that whistler mode interactions could not explain the isotropic precipitation of plasma sheet particles, investigators in the 1970s concentrated on sources of electrostatic wave energy. There are two important developments from the decade of which we take note. The first concerns direct observations of broadband electrostatic noise all along magnetic field lines connecting the auroral ionosphere to the equatorial plasma sheet.⁴¹ The amplitudes of observed waves are of sufficient intensity to drive strong pitch-angle scattering. The second development concerns the theoretical recognition of the role played by cold plasma for making available free energy contained in anisotropic pitch-angle distributions. Cold plasma, of ionospheric origin, in the plasma sheet can produce velocity space gradients in the total distribution functions ($\partial f / \partial v_{\perp} > 0$) that are unstable to the growth of ($N + 1/2$) electron cyclotron waves,⁴² and lower hybrid ion waves.⁴³ Numerical studies show that such waves are unstable over restricted ranges of parameter space. Measuring low density, cold plasma embedded in a hot plasma sheet is experimentally difficult. A successful measurement of the cold plasma component will be a critical requirement for future understanding of plasma sheet processes.

40. Williams, D. J., and Lyons, L. R. (1974) The proton ring current and its interactions with the plasmapause: storm recovery phase, J. Geophys. Res. 79:4195.

41. Gurnett, D. A., and Frank, L. A. (1977) A region of intense plasma wave turbulence on auroral field lines, J. Geophys. Res. 82:1031.

42. Young, T. S. T., Callen, J. D., and McCune, J. E. (1973) High frequency electrostatic waves in the magnetosphere, J. Geophys. Res. 78:1082.

43. Ashour-Abdalla, M., and Thorne, R. M. (1978) Toward a unified view of diffuse auroral precipitation, J. Geophys. Res. 83:4755.

4. ELECTRICAL COUPLING OF THE MAGNETOSPHERE AND IONOSPHERE

Before discussing the electrodynamics of the high-latitude ionosphere, it is useful to review briefly the theory of magnetosphere-ionosphere coupling. Vasyliunas⁴⁴ has developed a theoretical model that illustrates the physical laws describing how magnetospheric convection couples with the ionosphere. The model is presented in Figure 13 in the form of a closed loop of equations (straight lines), and of quantities to be determined (boxes). External sources of particles, cross-magnetospheric

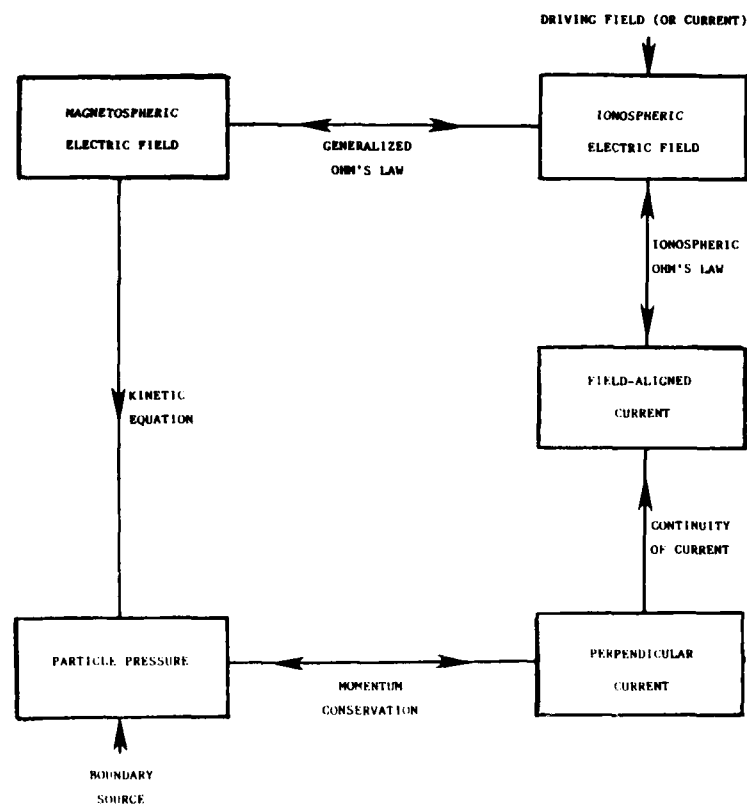


Figure 13. Outline of Self-Consistent Calculation of Magnetospheric Convection⁴⁴

44. Vasyliunas, V. M. (1970) Mathematical models of magnetospheric convection and its coupling to the ionosphere, in Particles and Fields in the Magnetosphere, B. M. McCormac, Ed., D. Reidel Co., Dordrecht, Holland, p. 60.

potentials, neutral winds in the ionosphere, and so forth, are imposed boundary conditions. Because the loop of equations is self-consistently closed, it can be entered at any point. Let us assume that we have an initial idea about the distribution of magnetospheric electric fields and particles.

(a) First link: with knowledge of the electric field, we calculate the motion and distribution of protons and electrons in the magnetosphere, and, hence, the total plasma pressure at any point;

(b) Second link: from the plasma pressure gradients we calculate the components of the electric current perpendicular to the magnetic field. That is, from the force balance equation

$$\vec{\nabla} p = \vec{j} \times \vec{B} \quad (30)$$

we calculate

$$\vec{j}_{\perp} = \frac{\vec{B} \times \vec{\nabla} p}{B^2} \quad (31)$$

For simplicity, we have assumed that the pressure is isotropic.

(c) Third link: by calculating the divergence of the perpendicular current, and averaging over each flux tube, we obtain (j_{\parallel}) the field-aligned currents flowing between the magnetosphere and the ionosphere.

$$\frac{1}{B^2} (\vec{j}_{\perp} \cdot \vec{\nabla} B) = -\frac{1}{B} \vec{\nabla}_{\perp} \cdot \vec{j}_{\perp} \quad (32)$$

(d) Fourth link: from the requirement that these field-aligned currents be closed by perpendicular ohmic currents in the ionosphere, we obtain the configuration of the electric field in the ionosphere. The continuity of ionospheric current requires that

$$\vec{\nabla} \cdot \vec{I} = j_{\parallel} \sin \chi \quad (33)$$

where I is the height integrated current and χ the inclination of magnetic field lines. In the ionosphere

$$\vec{I} = \vec{E} \cdot (\vec{E} + \vec{\nabla}_n \times \vec{B}) \quad (34)$$

where $\underline{\Sigma}$ is the height integrated conductivity tensor and \vec{V}_n is the neutral wind velocity.

(e) Fifth and final link: the ionospheric electric field can be mapped into the magnetosphere, and the requirement that it agree with the magnetospheric electric field assumed at the outset determines the field, and thus closes the system of equations. Except near discrete arcs, the mapping may be done by assuming that magnetic field lines are equipotentials. There is empirical evidence suggesting a functional relationship between j in discrete arcs and field-aligned potential drops.⁴⁵ We note in passing that the Rice University group has successfully simulated the ionospheric features of a magnetospheric substorm using this model.^{46,47}

From Eqs. (33) and (34) it is clear that measurements of \vec{E} and j are critical for understanding the magnetosphere-ionosphere circuit. Measurements of precipitating particle fluxes are needed to (1) understand spatial variation in $\underline{\Sigma}$, (2) identify the dominant carriers of j , (3) calculate field-aligned potential drops, and (4) help distinguish between topologically different regions.

5. HIGH-LATITUDE ELECTRIC FIELDS

Electric fields at ionospheric altitudes are measured from potential differences between the ends of extended booms on satellites⁴⁸ and from the $\vec{E} \times \vec{B}$ drifts of cold plasma.⁴⁹ In principle, j can be determined from particle fluxes. With present technology, full distribution functions of ions and electrons cannot be measured with sufficient accuracy. For this reason, highly sensitive triaxial

15. Lyons, F. R., Evans, D. S., and Lundin, R. (1979) An observed relationship between magnetic field aligned electric fields and downward electron energy fluxes in the vicinity of auroral forms, J. Geophys. Res. 84:457.
16. Harel, M., Wolf, R. A., Reiff, P. H., Spiro, R. W., Burke, W. J., Rich, T. J., and Seidley, M. (1981) Quantitative simulation of a magnetospheric substorm, 1, model logic and overview, J. Geophys. Res. 86:2217.
17. Harel, M., Wolf, R. A., Spiro, R. W., Reiff, P. H., Burke, W. J., Rich, T. J., and Seidley, M. (1981) Quantitative simulation of a magnetospheric substorm, 2, comparison with observations, J. Geophys. Res. 86:2217.
18. Fiksel, L. A. (1967) Theory of electric field measurements conducted in the ionosphere with electric probe, Space Sci. Rev. 7:239.
19. Hanson, W. B., and Heelis, R. A. (1975) Techniques for measuring bulk gas cation flow: satellite, Space Sci. Inst. 1:193.

fluxgate magnetometers⁵⁰ are used to determine j from magnetic deflections. Particle fluxes, in approximately the energy range 10 eV to 30 keV, are measured by means of continuous channel electron multipliers (channeltrons) placed behind electrostatic energy-analyzers.⁵¹

It is useful to explain the format of high-latitude data presented in the following subsections by providing an example of the simplest kinds of electric fields and magnetic field deflections expected to be measured by instrumentation on a polar-orbiting satellite. Figure 14a shows the trajectory of a satellite in circular polar orbit with the ascending node at the dusk (1800 LT) meridian. We define a satellite centered coordinate system; \hat{X} is positive along the satellite velocity; \hat{Z} is positive toward local nadir; \hat{Y} completes the right-hand system. In the dawn-dusk meridian, Y is positive in the antisunward direction. At high latitudes in the northern (southern) hemisphere, we approximate \bar{B} as being along the $+(-) Z$ axis. Figure 14a also shows dusk-to-dawn electric fields in the auroral ovals, and uniform dawn-to-dusk electric fields across the polar caps. The convective electric field reverses directions near the poleward boundary of the auroral oval, and goes to zero at the equatorward boundary.

The governing equations are current continuity [Eq. (33)], Ohm's law [Eq. (34)] and the Maxwell equation

$$\nabla \times \bar{B} = \mu_0 \bar{j} \quad (35)$$

In the infinite current sheet approximation, these equations may be combined to eliminate \bar{j} , and reduce to

$$\frac{\partial}{\partial x} (\bar{B}_y - \mu_0 p E_X) = 0 \quad (36)$$

where \bar{B}_y is the deflection of the magnetic field due to j , and $\mu_0 p$ is the height-integrated Pedersen conductivity.⁵² Except near local noon at the dayside cusp, and near local midnight at the Harang discontinuity where there are significant

50. Armstrong, J., and Zmuda, A. J. (1973) Triaxial magnetic measurements of field aligned currents at 300 km in the auroral region: initial results, J. Geophys. Res. 78:6302.

51. Frank, L. A. (1967) Initial observations of low-energy electrons in the earth's magnetosphere with OGO-3, J. Geophys. Res. 72:135.

52. Snidby, M., Burke, W. J., Kelley, M. C., Saffelos, N., Gussenhoven, M. S., Hardy, D. A., and Rich, F. J. (1980) Effects of high latitude conductivity on observed convection electric fields and Birkeland currents, J. Geophys. Res. 85:6311.

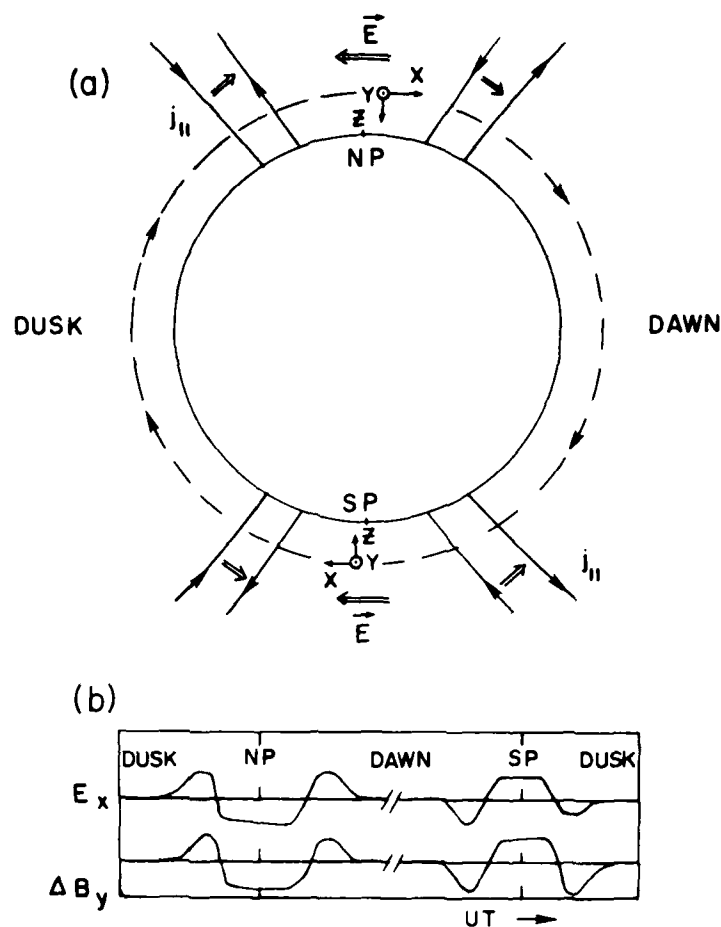


Figure 14. (a) Field-Aligned Currents and Electric Fields as Seen by a Polar-Orbiting Satellite in the Dawn-Dusk Meridian. (b) Idealized Electric Field and Magnetic Perturbation Measurements

divergences of the ionospheric Hall current,⁵³ Eq. (36) is a very useful approximation. It tells us that for a uniformly conducting ionosphere, fluctuations in the transverse magnetic field component should track variations in the meridional component of the electric field. Deviations from correlated variations are due to the

53. Rostoker, G. (1980) Magnetospheric and ionospheric currents in the polar cap and their dependence on the B_y component of the interplanetary magnetic field, *J. Geophys. Res.* 85:4167.

presence of conductivity gradients. Figure 14b is a plot of E_X and ΔB_Y expected over a full orbit assuming a uniform ionospheric conductivity. Positive (negative) slopes in ΔB_Y correspond to regions of current into (out of) the ionosphere. Thus, due to the divergence of ionospheric Pedersen currents, a field-aligned current (FAC) should flow into the ionosphere at the equatorward boundary of the dusk-side oval and out at the poleward boundary. The morning side oval currents have the opposite polarity. If there are significant Pedersen currents across the polar cap, the poleward FAC system should be of greater intensity than the equatorward system.

In the following subsections, ΔB_Y is given as a function of time rather than distance. Since satellites at ionospheric altitudes travel at speeds of ~ 7 km/sec, Eq. (35) can be transformed to give a convenient expression for j

$$j \left(\frac{\mu A}{m^2} \right) = 0.113 \frac{\partial \Delta B_Y \text{ (nT)}}{\partial t \text{ (sec)}} \quad (37)$$

A current of $1 \frac{\mu A}{m^2}$ corresponds to a locally unbalanced flux of $\sim 10^9 / \text{cm}^2 \text{ sec}$.

Finally, in both the polar cap and the auroral oval we refer to small- and large-scale structures. Small-scale structures have latitudinal dimensions of a few tens of kilometers or less. They are traversed by satellites in a few seconds. Discrete arcs and inverted-Vs are examples of small-scale structures. Large-scale systems have latitudinal dimensions greater than 100 km. The E field and field-aligned current systems shown in Figure 14b are of large scale.

6. POLAR CAP ELECTRODYNAMICS

This section treats three topics: (1) large-scale electric field patterns, (2) electron precipitation morphologies, and (3) characteristics of discrete, sun-aligned arcs in the polar cap. Here we use the term "polar cap" to designate the portion of the high-latitude ionosphere containing only open magnetic field lines. Precipitating particles on these field lines should be of direct magnetosheath origin. Except possibly during periods of northward interplanetary magnetic field, cold ionospheric plasma should convect in the antisunward direction under the influence of a dawn-to-dusk electric field.

6.1 Large-Scale Electric Field Patterns

Table 1 lists the six polar orbiting satellites launched to date that were capable of measuring ionospheric electric fields. Data from the double-probe experiment

Table 1. Satellites Capable of Measuring Electric Fields

SATELLITE	LAUNCH DATE	INCLINATION	INITIAL APOGEE (km)	TYPE INSTRUMENT
Injun 5	Aug 1968	81 ⁰	2550	double probe
OGO-6	June 1969	82 ⁰	1600	double probe
AE-C	Dec 1973	68 ⁰	4000	drift meter
AE-D	Oct 1975	90 ⁰	4000	drift meter
S3-2	Dec 1975	96 ⁰	1550	double probe
S3-3	Aug 1976	98 ⁰	8050	double probe

on Injun 5 confirmed the existence of convective reversals near the poleward boundaries of the auroral oval. An inclination of 68° allowed the Atmospheric Explorer (AE)-C driftmeter to measure convective drifts in the oval, but usually not in the polar cap. The AE-D satellite had an inclination of 90°, but failed about four months after launch. Initially, the orbit was close to the noon-midnight meridian; it then precessed toward dawn-dusk. Because of the high altitude of S3-3, its apogee data have been most useful for identifying the small-scale features of auroral arc and inverted-V phenomena. The OGO-6 and S3-2 satellites spent sufficient periods of time near the dawn-dusk meridian to identify the main large-scale features of polar-cap convection.

Two examples of E_x measured by OGO-6 at northern (summer) high latitudes are given in Figure 15. Except for small-scale variations, the main features of the expected E_x patterns are found in the auroral oval. The example in the top

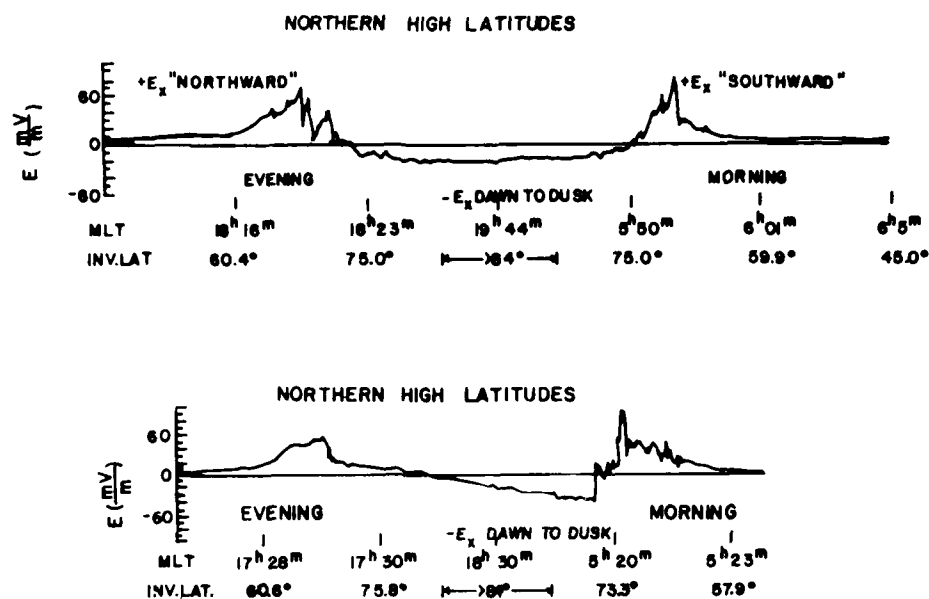


Figure 15. Two Examples of Large-Scale Electric Fields Measured by OGO-6

trace is consistent with a uniform dawn-to-dusk electric field across the polar cap. In the bottom trace, E_x has relatively high (low) values near the morning (evening) flank of the polar cap.

A simplified summary of large-scale electric field patterns identified by Heppner⁵⁴ is given in Figure 16.

- Type A: Uniform E_x across polar cap. These were observed by OGO-6 only in the northern (summer) polar cap.
- Type B: Strong E_x near the morning (evening) flank of the northern (southern) polar cap.
- Type C: Strong E_x near the evening (morning) flank of the northern (southern) polar cap.
- Type D: Strong E_x near the flank of polar cap with weak fields in the other flank.
- Type E: Weak E_x across the polar cap.

Figure 16. Summary of large-scale electric field patterns observed (away) structure.

54. Heppner, J. L. *U.S. National Academy of Sciences*, 77:1177, 1977.

CROSS-POLAR CAP
ELECTRIC FIELD PATTERNS

JUNE, 1969
OGO-6

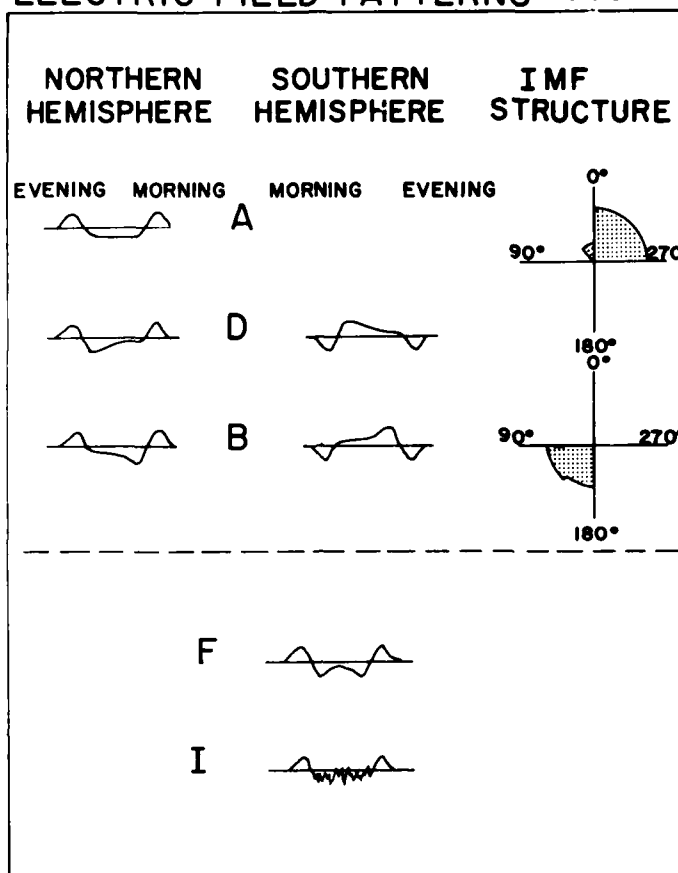


Figure 16. Types of Electric Field Patterns Observed by OGO-6, and Their Dependence on the Interplanetary Magnetic Field B_x and B_y .

During the last three months of 1976, the S3-2 orbit was close to the dawn-dusk meridian. Figure 17 is a scatter plot of Heppner's patterns observed in S3-2 data as a function of IMF B_x and B_y . It is seen that A and B types are found only when $B_y \sim 0$. For both OGO-6 and S3-2, A types are only found in the summer hemisphere, and are associated with the IMF polarity that tends to produce strong E fields along the evening flank of the polar cap. The occurrence ratio of A to B was 2:1 in S3-2 data; the A to D ratio was 3:1 in June 1969, OGO-6 data. The dependence of D types on B_y (upper right plot) agrees with OGO-6. The type F patterns were found when $B_y \sim 0$. The distribution of B, D, and F patterns tends

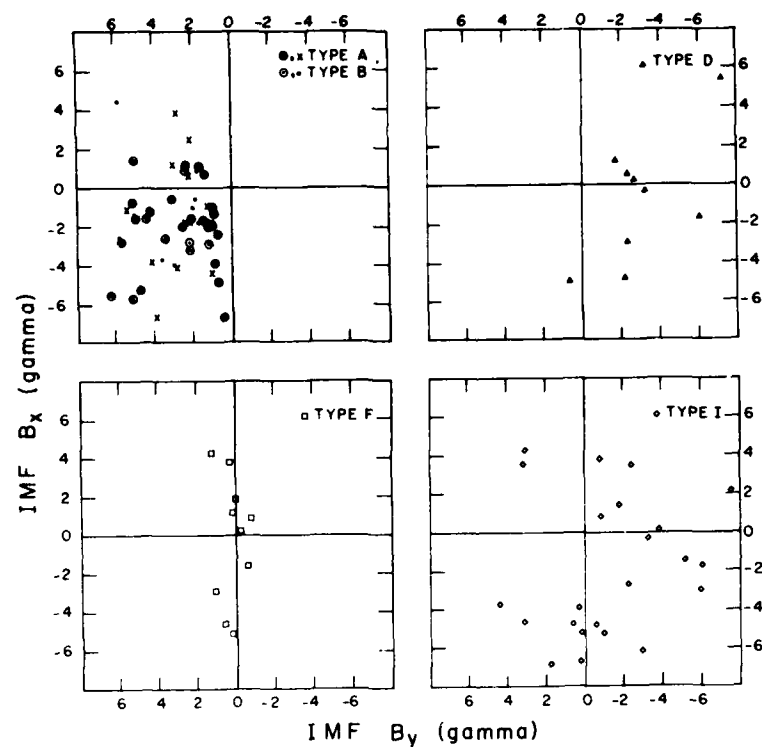


Figure 17. Scatter Plot of Convective Electric Field Patterns Observed by S3-2 as a Function of IMF B_x and B_y .

to confirm the critical role of B_z .⁵⁵ A survey of S3-2 measurements shows that A, B, D, and F types are found when $B_z < 0.5$ nT. Type I shows no correlation with B_x or B_y . The highly irregular electric fields are found only when $B_z > 0$. Type I patterns are discussed further in connection with polar-cap arcs.

An example of an E-field pattern that was found in approximately half of the summer polar-cap passes of S3-2, when $B_z = 0.7$ nT, is shown in Figure 18. During the S3-2 Rev 5215 southern high-latitude pass B_z was measured as 4.9 nT.⁵⁶ As expected for driving sunward convection in the auroral oval, E_x was directed

55. Friis-Christensen, E., Lassen, K., Wilhelm, J., Wilcox, J. M., Gonzalez, W., and Colburn, D. S. (1972) Critical component of the interplanetary magnetic field responsible for large geomagnetic events, *J. Geophys. Res.* 77:3371.

56. Burke, W. J., Kelley, M. C., Sagalyn, R. C., Smiddy, M., and Lai, S. T. (1979) Polar cap electric field structure with a northward interplanetary magnetic field, *Geophys. Res. Lett.* 6:21.

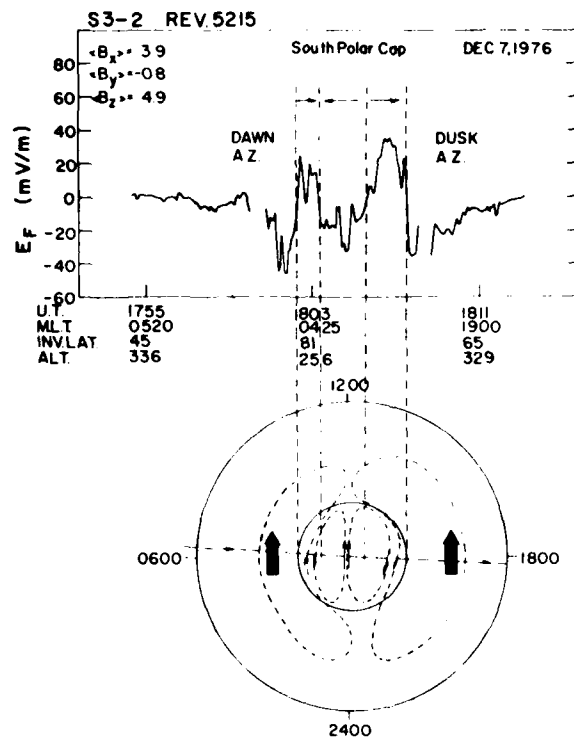


Figure 18. Example of Sunward Convection and a Dusk-to-Dawn Electric Field in the Central Polar Cap During a Period of Northern IMF. The dawn and dusk sides of the auroral zone (A.Z.) are indicated. Ionospheric plasma flow vectors are indicated in the bottom panel by arrows

from dusk to dawn. At the poleward boundary of the oval, E_N reversed polarity, becoming dawn-to-dusk near the morning and evening flanks of the polar cap. Within the central polar cap, E_N was directed from dusk to dawn. Sunward convection in the central polar cap is inconsistent with a viscous interaction model. It was theoretically anticipated as a consequence of the magnetic merging model by Russell.⁵⁷ Sunward convection in the summer polar cap during periods of

57. Russell, C. T. (1972) The configuration of the magnetosphere, in Critical Problems of Magnetospheric Physics, E. R. Dyer, Ed., National Academy of Science, Washington, D. C., p. 1.

northward B_Z is consistent with ground magnetometer⁵⁸ and laboratory simulation⁵⁹ results.

The cross-polar-cap potential $\Delta\Phi_{pc}$ can be derived from satellite electric field measurements, and is an important parameter for magnetospheric modeling. This potential (in volts) gives the rate (in webers/sec) that magnetic flux is transferred from the day to the night side of the magnetosphere. Based on two weeks of OGO-6 data, Heppner⁶⁰ found that the average $\Delta\Phi_{pc}$ increased from 20 to 100 kV as the magnetic index Kp increased from 0 to 6. There were individual cases in which $\Delta\Phi_{pc}$ significantly exceeded 100 kV.

Reiff et al.⁶¹ analyzed 32 measurements of $\Delta\Phi_{pc}$ from AE-C and AE-D as a function of various solar wind and IMF parameters. To calculate merging rates that account for compression of the IMF in the magnetosheath, the value of B at the magnetopause was set at the lesser of 8 times its solar wind value, or 60 nT. The latter value was taken as typical of the earth's field near the subsolar magnetopause. Although the best agreement was found with theoretical merging rates, a high correlation was found with Akasofu's⁶² ϵ parameter. Figure 19 shows that in the AE measurements $\Delta\Phi_{pc}$ varied from 30 to 150 kV. This implies that 30 kV cannot be accounted for by merging. Such a potential greatly exceeds the potential across the boundary layer theoretically estimated by Hill,⁶³ and measured at ionospheric altitudes by Smiddy et al.⁵² The upper limit of ~ 150 kV is much less than the cross-magnetosphere potential drop ($\Delta\Phi_{sw}$) in the solar wind. With $V_s = 400$ km/sec, and $B_Z = -5$ nT, the Y component of the electric field in the solar wind is 2 mV/m ($=12.8$ kV/ R_E). For a magnetospheric diameter of $30 R_E$ at the dawn-dusk meridian, $\Delta\Phi_{sw} = 384$ kV.

-
- 58. Maezawa, K. (1976) Magnetospheric convection induced by the positive and negative Z components of the interplanetary magnetic field: quantitative analysis using polar cap magnetic records, J. Geophys. Res. 81:2289.
 - 59. Podgorny, I. M., Dubinin, E. M., and Potanin, Yu. N. (1978) The magnetic field on the magnetospheric boundary from laboratory simulation data, Geophys. Res. Lett. 4:207.
 - 60. Heppner, J. P. (1977) Empirical models of high-latitude electric fields, J. Geophys. Res. 82:1115.
 - 61. Reiff, P. H., Spiro, R. W., and Hill, T. W. (1981) Dependence of polar-cap potential drop on interplanetary parameters, J. Geophys. Res. 86:7639.
 - 62. Akasofu, S. -I. (1978) Interplanetary energy flux associated with magnetospheric substorms, Planet. Space Sci. 27:425.
 - 63. Hill, T. W. (1979) Generation of the magnetospheric electric field, in Quantitative Modelling of Magnetospheric Processes, W. P. Olson, Ed., AGU Monograph 21, Washington, D. C., p. 297.

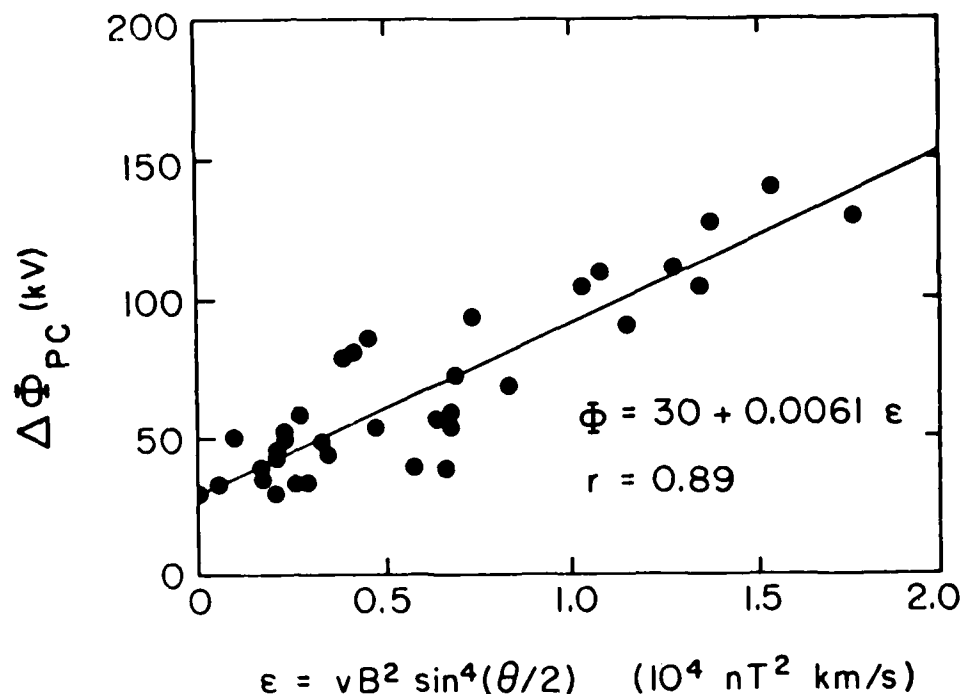


Figure 19. Cross-Polar-Cap Potential as a Function of Solar Wind Parameter ϵ ⁶¹

6.2 Polar Cap Precipitation

Particle fluxes into the polar ionosphere are conveniently divided into high and low energy components. Energetic particles from solar flares can seriously disrupt the polar ionosphere; these are important during magnetic storm periods. The flux levels of low-energy protons in the polar cap are below the sensitivity levels of existing detectors. Winningham and Heikkilä⁶⁴ identified three classes of low-energy electron precipitation: polar rain, polar showers, and polar squalls.

Polar rain is a relatively uniform type of precipitation that can fill the entire polar cap. Particles have mean thermal energies of ~ 100 eV, and are isotropically distributed outside the atmospheric loss cone. The energy fluxes carried by these particles range from 10^{-2} to 10^{-3} erg/cm² sec, two to three orders of magnitude less than typical auroral energy fluxes. The highest energy fluxes for polar rain

64. Winningham, J. D., and Heikkilä, W. J. (1974) Polar cap auroral electron fluxes observed with Isis 1, *J. Geophys. Res.*, 79:949.

occur during periods of geomagnetic activity.⁶⁵ Figure 20 is a plot of precipitating electron spectra, measured in the dayside cusp and in the polar rain. The similarity in spectral shape suggests that polar rain particles are of direct magnetosheath origin. Particle fluxes measured in the lobes of the magnetotail indicate

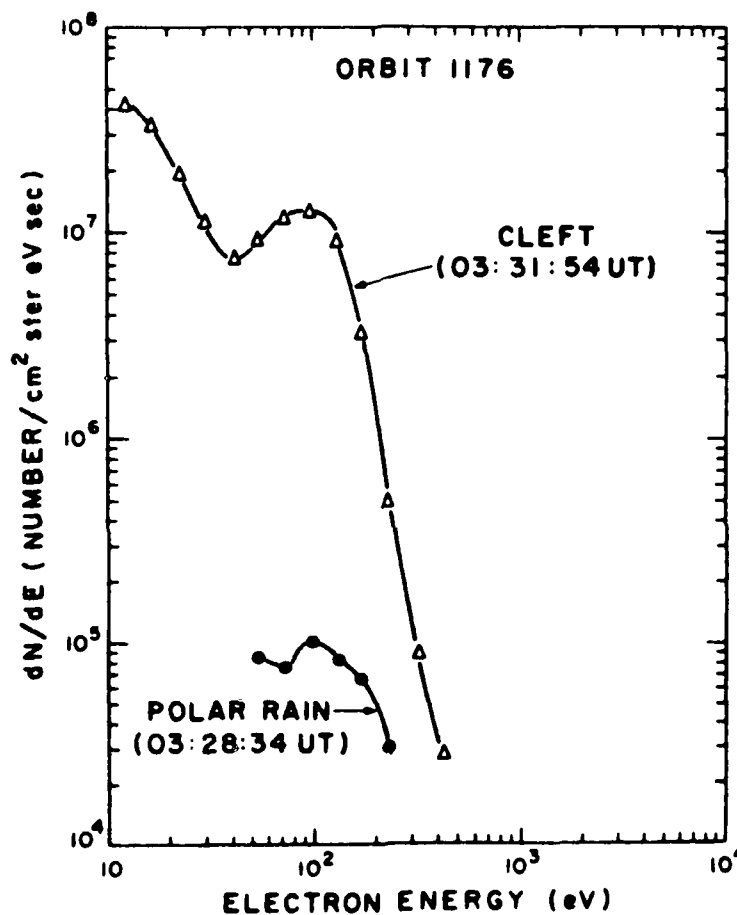


Figure 20. Typical Differential Spectra for the Polar Rain and Cleft Precipitation Observed on Orbit 1176 on 15 May 1969

65. Meng, C. -I., and Kroel, H. W. (1977) Intense uniform precipitation of low-energy electrons over the polar cap, J. Geophys. Res. 83:2305.

that polar rain electrons enter the magnetosphere at a great distance downstream from the earth. The efficiency of the entry process is modulated by the polarity of the IMF. Yaeger and Frank⁶⁶ found that fluxes of soft electrons in the northern lobe of the tail increased by more than an order of magnitude when the IMF was in an away ($B_x < 0$) sector. There is also evidence suggesting a B_x influence. Meng et al.⁶⁷ found that the intensity of polar rain fluxes is strongest near the flank of the polar cap along which convection is strongest.

Polar showers are characterized by locally enhanced fluxes of precipitating electrons with mean energies of ~ 1 keV. These electron structures are embedded in broader regions of polar rain. They are thought to be responsible for sun-aligned arcs in the polar cap, and are discussed further under that heading.

Polar squalls are described by Winningham and Heikkila⁶⁴ as localized, intense fluxes of electrons that have undergone field-aligned accelerations of several keV. They are found in the polar cap during geomagnetic storms. Foster and Burrows^{68, 69} have reported observing fluxes of electrons into the polar cap that are spectrally identical to those found in polar squalls. These fluxes, however, were observed to be widely and uniformly distributed over the polar cap. Like squall particles, they were observed during the recovery phases of magnetic storms. These fluxes also appear to be modulated by the polarity of the IMF. While intense fluxes of keV electrons were measured in the northern polar cap, only polar rain was detected in the southern hemisphere. Figure 21 is a plot of particle fluxes measured in the polar rain and extended squalls by ISIS 2, and nearly simultaneous measurements of electron fluxes in the magnetosheath and the tail lobe from VELA 5. Foster and Burrows⁶⁹ argue from the near isotropy of the keV particles in the polar cap, and the absence of keV electrons in the magnetosheath, that the electrons were accelerated along magnetic field lines at a great distance from the earth in the magnetosphere.

-
- 66. Yaeger, D. M., and Frank, L. A. (1976) Low-energy electron intensities at large distances over the earth's polar cap, J. Geophys. Res. 81:3966.
 - 67. Meng, C. -I., Akasofu, S. -I., and Anderson, K. A. (1977) Dawn-dusk gradient of the precipitation of low-energy electrons over the polar cap and its relation to the interplanetary magnetic field, J. Geophys. Res. 83:5271.
 - 68. Foster, J. C., and Burrows, J. R. (1976) Electron fluxes over the polar cap 1, intense keV fluxes during poststorm quieting, J. Geophys. Res. 81:6016.
 - 69. Foster, J. C., and Burrows, J. R. (1977) Electron fluxes over the polar cap 2, electron trapping and energization on open field lines, J. Geophys. Res. 82:5165.

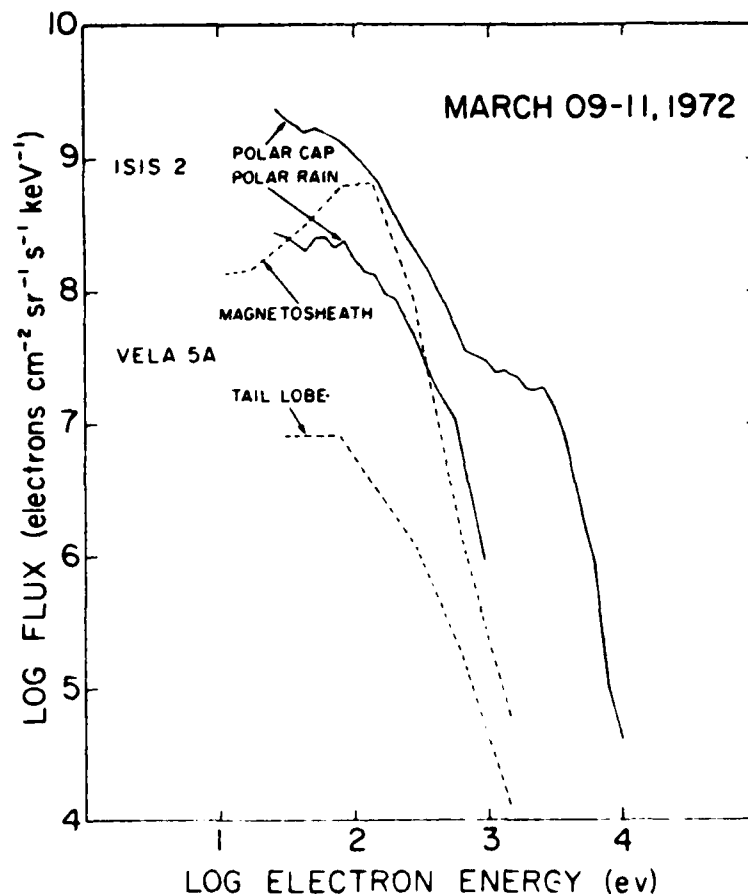


Figure 21. Differential Electron Energy Spectra Measured in the Polar Cap (Solid Curves), and in the Tail Lobe and the Magnetosheath (Dashed Curves). The magnetosheath measurement was made at ~ 13 h on 9 March, the tail lobe measurement at ~ 9 h on 11 March, the polar cap measurement at ~ 16 h on 10 March, and the polar rain measurement at ~ 11 h on 9 March. The polar cap spectra display a more or less pronounced high-energy tail relative to the magnetosheath²⁷

6.3 Polar Cap Arcs

Investigations of discrete arcs in the polar cap have shown that polar cap arcs tend to be sun-aligned, and are most frequently observed during periods of magnetic quieting, when the IMF has a northward component.⁷⁰ Visible arcs are caused by precipitating electrons with energies of < 2 keV. Another class of subvisual arcs

70. Ismail, S., Wallis, D. D., and Cogger, L. I. (1977) Characteristics of polar sun-aligned arcs, *J. Geophys. Res.* 82:4741.

are produced at F-layer altitudes by electrons with energies of a few hundred eV.⁷¹ Here we illustrate many of the known characteristics of polar-cap arcs using data from the USAF satellites S3-2 and DMSP (Defense Meteorological Satellite Program). At the times of interest, both satellites were in orbits close to the dawn-dusk meridian. S3-2 measured E_X , $\perp B_Y$ (described above), and fluxes of electrons with energies between 50 eV and 17 keV. DMSP satellites are three-axis stabilized, and are in circular, sun-synchronous orbit at an altitude of 840 km. All DMSP satellites are equipped with scanning, optical imagers.⁷² Some, but not all, are also equipped with spectrometers that look toward local zenith, and measure fluxes of electrons with energies between 50 eV and 20 keV.

Figure 22 is a cartoon that represents, in magnetic latitude and local time, composites of visible imagery from DMSP/F1 and DMSP/F2 taken over the northern hemisphere during a period of magnetic quieting on 12 December 1977. Solid, straight lines give the portions of F2 trajectories during which electron data were taken. To the right of each cartoon, the hourly average values of IMF B_Y and B_Z are represented. During the initial period of southward B_Z , the polar cap was clear of visible emissions, and only uniform, polar rain fluxes were detected. Approximately one hour after the IMF turned northward, sun-aligned arcs were found in the polar cap. Polar cap arcs persisted until the IMF again turned southward. An hour after a second northward turning of B_Z , arcs returned to the polar cap.⁷³ The sun-aligned arcs were embedded in a region of high-density ($\sim 0.1 \text{ cm}^{-3}$) polar rain. Within the arc, the up-looking DMSP spectrometer detected three spectral components, a cold (100 eV) high-density (1.5 cm^{-3}) population, a peaked primary distribution with a temperature of 350 eV that had been accelerated through a potential drop of ~ 750 volts, and a secondary and/or degraded primary population. Burch et al.⁷⁴ found that the low-energy component was highly field-aligned over polar showers. The secondary and accelerated primary populations were nearly isotropic in pitch angle.

Figure 23 gives a plot of E_X , $\perp B_Y$, the directional flux of electrons ($\text{cm}^{-2} \text{ sec}^{-1} \text{ ster}^{-1}$), and electron pitch angles measured during S3-2 Rev 5231 as functions of

-
- 71. Weber, E. J., and Buchau, J. (1981) Polar cap F-layer auroras, Geophys. Res. Lett. 8:125.
 - 72. Eather, R. H. (1979) DMSP calibration, J. Geophys. Res. 84:4134.
 - 73. Hardy, D. A., Burke, W. J., and Gussenhoven, M. S. (1981) DMSP optical and electron measurements in the vicinity of polar cap arcs, J. Geophys. Res. 87:2413.
 - 74. Burch, J. T., Fields, S. A., and Heelis, R. A. (1979) Polar cap electron acceleration regions, J. Geophys. Res. 84:5863.

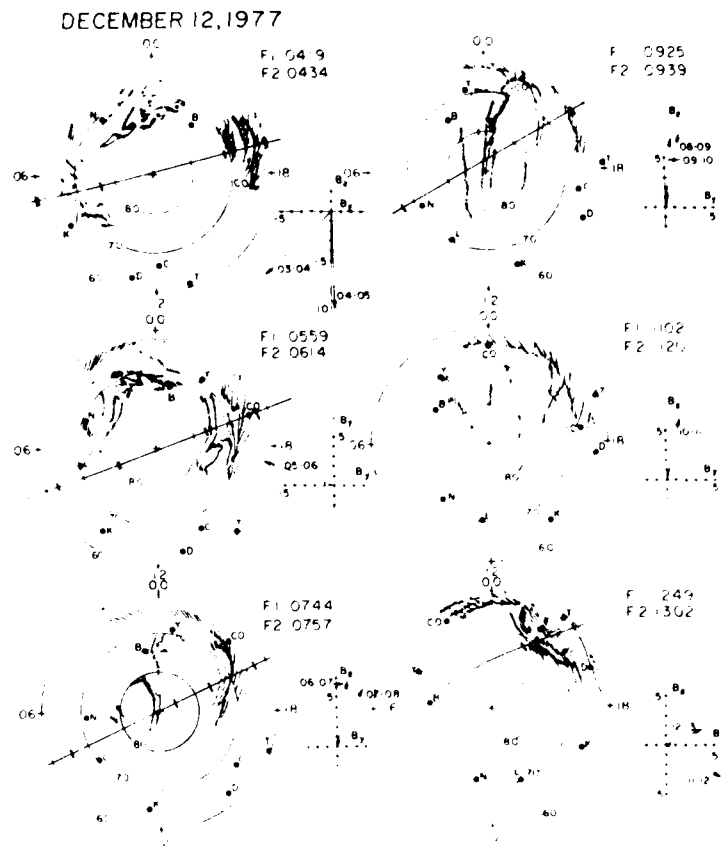


Figure 22. Cartoon Representation of Sequential DMSP High-Latitude Imagery on 12 December 1977

invariant latitude, magnetic local time, and altitude. The pass occurred while the satellite was near apogee over the north polar cap where it passed within 1° of the magnetic pole along the dawn-dusk meridian. The IMF X , Y , and Z components were -3.7 , 3.8 , and 7.4 nT, respectively. As compared with the idealized measurements of Figure 14b, E_N , and ΔB_y , were highly irregular. Recall that in the northern hemisphere, E_N positive corresponds to sunward convection; i_z is out of the ionosphere in regions where ΔB_y has a negative slope. Eight regions of negative slope in ΔB_y accompanied by enhanced electron fluxes are noted in Figure 23. As evidenced by their being embedded in polar rain, Events 3 through 7 lie in the polar cap.

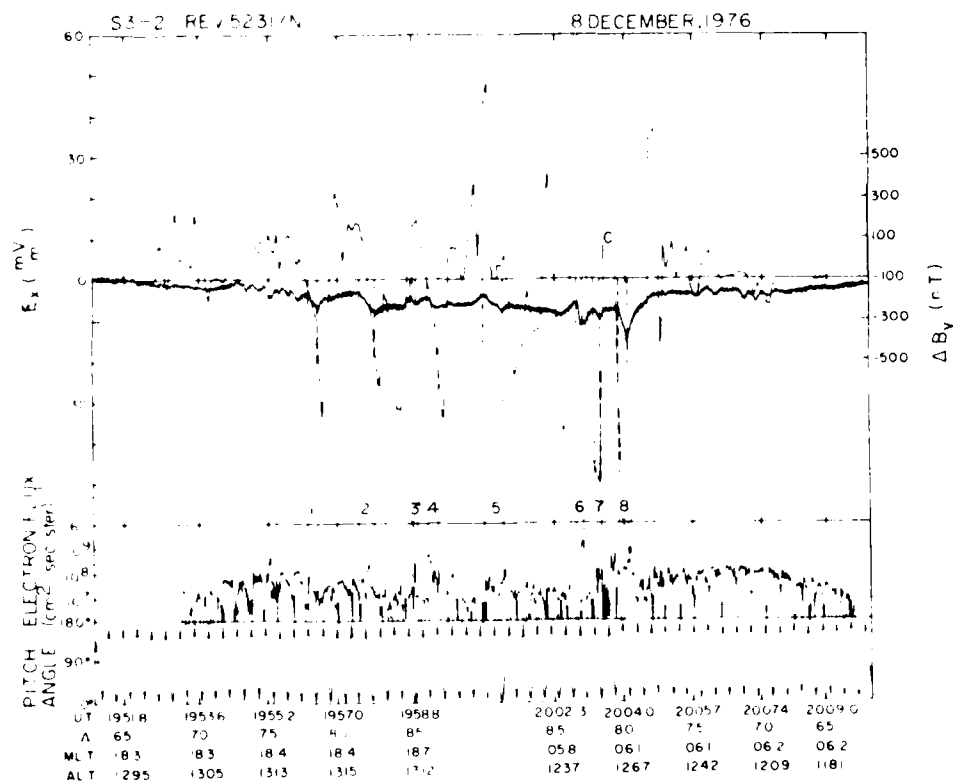


Figure 23. The Dawn-to-Dusk Electric Field Component, and the Transverse Magnetic Field Deflection (Heavy Line, Top Panel). The directional electron flux and pitch angles (bottom panel). Data were taken over the winter polar cap with IMF B_z northward

Event 6 has been analyzed in detail by Burke et al.⁷⁵ It was shown that the field-aligned current out of the ionosphere had an intensity of $2.8 \mu A/m^2$, and was carried by electrons with a temperature of 200 eV that had been accelerated through a potential drop of ~ 1 kV. A nearly isotropic pitch angle distribution of electrons across Event 6 suggests a field-aligned potential drop extending for large distances along \vec{B} . The measured electron energy fluxes of 2.5 ± 0.5 ergs/cm² sec ster were sufficient to produce a visible arc. Figure 24 gives an idealized, two-dimensional projection of the electric fields and currents associated with Event 6.

75. Burke, W. J., Gussenhoven, M. S., Kelley, M. C., Hardy, D. A., and Rich, F. J. (1982) Electric and magnetic field characteristics of discrete arcs in the polar cap, *J. Geophys. Res.* 87:2431.

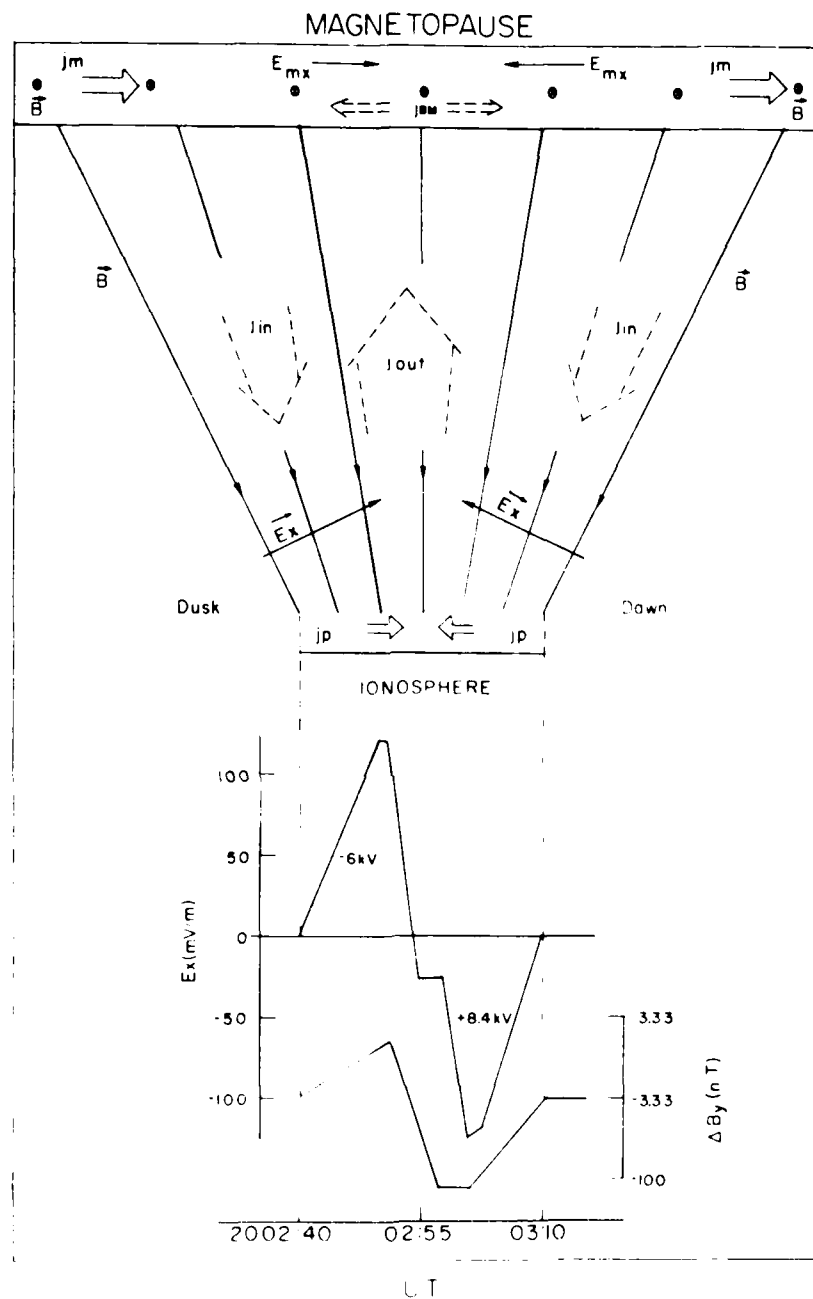


Figure 24. Idealized Two-Dimensional Projection of Electric Fields and Currents in the Vicinity of Event 6 in Figure 23

As predicted by Lyons,^{76,77} the arc is in a region of negative electric field divergence.

7. AURORAL OVAL ELECTRODYNAMICS

The auroral oval is a region of closed magnetic field lines mapping through the plasma sheet. Ionospheric plasma convection should be mostly in the sunward direction. Near local midnight (noon) strong equatorward (poleward) convection components are expected.

The stock-in-trade vocabulary of a contemporary auroral physicist is replete with terms such as "inverted-Vs," "double-layers," "diffuse aurora," "beams and conics," etc. These terms describe distinct auroral processes first reported in the 1970s.⁷⁸ These new phenomena defy adequate summation in this section. Here we consider three main topics (1) global auroral morphology, (2) phenomena associated with inverted-V events, and (3) substorms. Under the heading of global morphology, we treat the systematics of large-scale, field-aligned current systems, and the equatorward boundary of diffuse auroral precipitation.

7.1 Global Field-Aligned Currents

The average, global field-aligned current (FAC) system for periods of high and low magnetic activity is shown in Figure 13. Hiiima and Potemra⁷⁹ define Region 1 (2) as a region of FAC near the poleward (equatorward) portion of the auroral oval. In the evening sector, current flows into the ionosphere in Region 2, and out in Region 1. The polarity of current flow is reversed in the morning sector. The intensities of these currents is of order $1 \mu A/m^2$. Currents out of the ionosphere are carried mostly by precipitating electrons. It is believed that cold electrons moving from the ionosphere to the magnetosphere carry the current into

- 76. Lyons, L. R. (1980) Generation of large-scale regions of auroral currents, electric potentials, and precipitation by the divergence of the convection electric field, *J. Geophys. Res.*, 85:17.
- 77. Lyons, L. R. (1981) Discrete auroras: the direct result of an inferred high-altitude generating potential distribution, *J. Geophys. Res.*, 86:1.
- 78. Møzer, T. S., Cattell, C. A., Deaton, M. L., Lysak, R. L., Torrerin, M., and Forbert, R. B. (1980) Satellite observations and theories of low altitude auroral particle acceleration, *Space Sci. Rev.*, 27:155.
- 79. Hiiima, T., and Potemra, T. A. (1979) Large-scale characteristics of field-aligned currents associated with substorms, *J. Geophys. Res.*, 84:599.

the ionosphere. Klumpar⁸⁰ found that the equatorward boundary of Region 2 is co-terminus with diffuse auroral electron precipitation in the post-midnight sector. In the evening sector, Region 2 extends $\sim 2^\circ$ equatorward of the electron precipitation boundary.

Near local midnight and noon, large-scale FACs are their most complex. Figure 25 shows that near midnight the morning-side Region 1 current overlaps

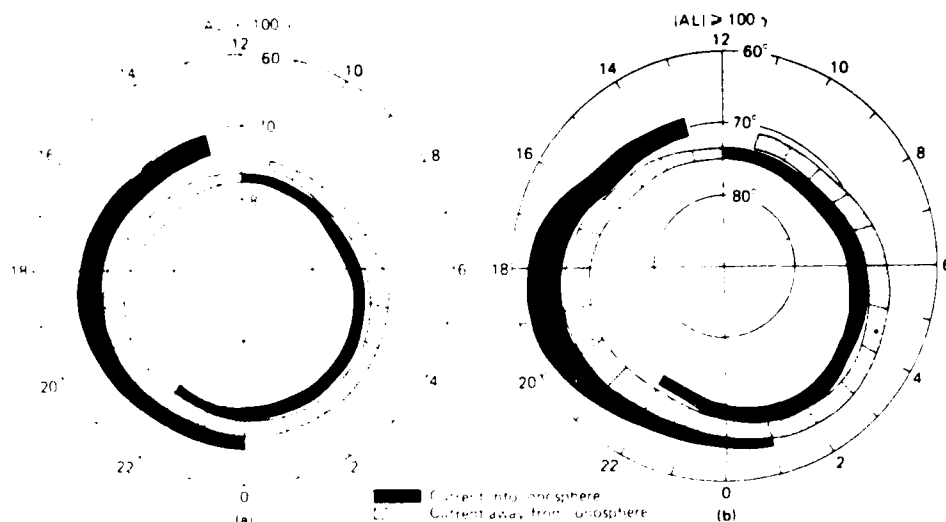


Figure 25. A Summary of the Distribution and Flow Directions of Large-Scale Field-Aligned Currents Determined From (a) Data Obtained From 439 Passes of Triad During Weakly Disturbed Conditions, and (b) Data Obtained From 366 Triad Passes During Active Periods

the evening-side Region 1. No simultaneous electric field and magnetic field measurements have been reported yet from this region. It is expected, however, that the morphology of these FACs can be understood in terms of latitudinal variations of the electric field just prior to local midnight. Maynard⁸¹ showed that in the late evening sector, the large-scale convective electric field is directed poleward in the equatorward part of the oval. It rotates through west across the Harang discontinuity, to equatorward in the poleward part of the oval. Pedersen currents driven in

80. Klumpar, D. M. (1979) Relationships between auroral particle distributions and magnetic field perturbations associated with field aligned currents, *J. Geophys. Res.* 84:6524.
81. Maynard, N. C. (1974) Electric field measurements across the Harang discontinuity, *J. Geophys. Res.* 79:1620.

the ionosphere converge from both sides on the Harang discontinuity. To maintain an overall divergence-free current system, current must flow into the ionosphere at both the equatorward and poleward boundaries of the oval, and out of the ionosphere near the Harang discontinuity. These are the essential features found near midnight in Figure 25.

In the vicinity of the dayside cusp, an extra FAC system has been observed poleward of Region 1. Its polarity is opposite to that of the nearby Region 1 current. In the northern (southern) hemisphere it appears only on the afternoon (morning) side of noon when IMF $B_y < 0$, and only on the morning (afternoon) side when IMF $B_y > 0$.⁸² Simultaneous electric and magnetic field measurements from the USAF satellite S3-2, in the region of the dayside cusp, suggest that the extra FAC system lies entirely on open, newly merged magnetic field lines that are being dragged toward the dusk or dawn flank of the polar cap.⁸³

7.2 The Equatorward Boundary of the Auroral Oval

In the previous section it was pointed out that the inner edge of the plasma sheet, or zero-energy Alfvén boundary, maps to the equatorward boundary of diffuse auroral precipitation. More than four thousand crossings of this boundary have been analyzed using data from an upward-looking electron spectrometer on the polar-orbiting USAF satellites DMSP/F2 and DMSP/F4. The corrected geomagnetic latitudes of the boundaries (Λ_{CGM}) were studied as functions of magnetic local time (MLT) and Kp. Kp is a 3 h index of magnetic activity compiled from a worldwide network of mid-latitude magnetometer stations. Results of linear correlation analyses

$$\Lambda_{CGM} = \Lambda_0 + \alpha Kp$$

82. McDiarmid, I. R., Burrows, J. R., and Wilson, M. D. (1979) Large-scale magnetic field perturbations and particle measurements at 1400 km on the dayside, *J. Geophys. Res.*, 84:1431.

83. Doyle, M. A., Rich, F. J., Burke, W. J., and Smiddy, M. (1981) Field-aligned currents and electric fields in the region of the dayside cusp, *J. Geophys. Res.*, 86:5656.

from available MLT sectors, are given in Tables 2 and 3 along with correlation coefficients. Using the magnetic field model of Fairfield and Mead,⁸⁴ the auroral boundaries were projected to the magnetospheric equatorial plane. Figure 26 is a plot of projected boundary positions (open circles), in comparison with predictions of the Volland-Stern electric field model³⁶ (solid line) and the injection boundary of Mauk and McIlwain⁸⁵ (dashed lines). Best fits are obtained for a shaping factor $\nu = 2$.

Table 2. Regression Coefficients for Auroral Boundaries in the Morning Sector

MLT	North				South			
	Λ_0	α	N	cc	Λ_0	α	N	cc
0400-0500	67.4	-1.35	171	-0.58				
0500-0600	67.8	-1.87	365	-0.75				
0600-0700	68.5	-1.96	403	-0.82	67.4	-1.67	376	-0.74
0700-0800	70.2	-2.15	367	-0.83	68.3	-1.97	411	-0.81
0800-0900					68.7	-1.88	302	-0.72
0900-1000					69.1	-1.64	217	-0.67

Table 3. Regression Coefficients for Auroral Boundaries in the Evening Sector

MLT	North				South			
	Λ_0	α	N	cc	Λ_0	α	N	cc
1600-1700					71.3	-1.19	107	-0.65
1700-1800					70.7	-1.20	256	-0.69
1800-1900	71.6	-2.00	103	-0.90	70.6	-1.60	327	-0.80
1900-2000	71.2	-1.96	426	-0.89	70.0	-1.82	447	-0.87
2000-2100	69.4	-1.85	452	-0.82	69.5	-1.89	345	-0.84
2100-2200	68.7	-1.66	556	-0.83				
2200-2300	68.3	-1.79	184	-0.63				

84. Fairfield, D. H., and Mead, G. D. (1975) Magnetospheric mapping with a quantitative geomagnetic field model, J. Geophys. Res. 80:535.

85. Mauk, B. H., and McIlwain, C. E. (1974) Correlations of Kp with substorm injected plasma boundary, J. Geophys. Res. 79:3193.

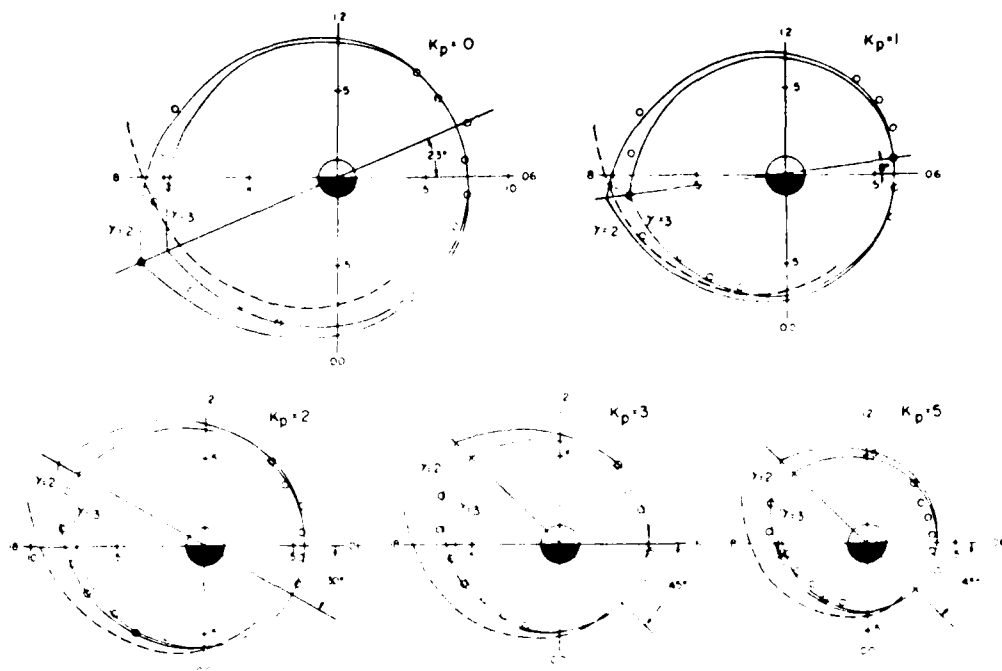


Figure 26. Volland-Stern Injection Boundaries for $\gamma = 2$ and $\gamma = 3$, Rotated to Fit the Inner Edge of the Plasma Sheet as Determined by the DMSP/F2 Auroral Boundaries, for Various K_p . The Mauk-McIlwain⁸⁵ injection boundary is also shown (dashed line)

Note that the stagnation points are offset from the dusk meridian. The offset angle ϵ_0 varies from 23° toward evening for $K_p = 0$, to 45° toward afternoon for $K_p = 5$. The potential distribution in the equatorial plane [Eq. (24)] takes the form

$$\Phi(L, \epsilon) = -B_0 R_E^2 \left[\frac{I_S}{I_S + 1} \sin(\epsilon - \epsilon_0) + \frac{1}{L} \right] \quad (33)$$

For $\gamma = 2$ the term $1/(I_S + 1)$ is empirically related to K_p

$$\frac{1}{I_S + 1} = (1.6 + 2.4 K_p) \cdot 10^{-4}$$

with a correlation coefficient of 0.97. Thus,

$$\Phi(L, \epsilon) = -B_0 R_E^2 [(1.6 + 2.4 K_p) 10^{-4} L^2 \sin(\epsilon - \epsilon_0) + \frac{1}{L}] \quad (34)$$

A further analysis⁸⁶ has been performed correlating the boundary data and hourly averaged solar wind and IMF measurements. The most significant results were obtained when Λ_{CGM} was correlated with the interplanetary electric field VB_Z for the hour preceding the boundary measurement, subject to the condition $B_Z \geq 1$ nT. Correlation parameters are summarized in Table 4. To compare the

Table 4. The Intercepts (Λ_0), Slopes, Correlation Coefficients (cc), and Sample Sizes (N) for the Linear Regression of the Boundary Location With VB_Z in Each Magnetic Local Time Zone, With a 1 h Delay in the Value of the Interplanetary Magnetic Field (IMF) Used

	North Pole					South Pole				
	MLT	Λ_0	Slope	cc	N	Λ_0	Slope	cc	N	
B _z > 1 nT	0400-0500	65.1	3.28	0.52	43					
	0500-0600	63.6	1.94	0.61	110					
	0600-0700	64.2	1.80	0.70	105	64.4	1.70	0.56	124	
	0700-0800	66.1	2.56	0.68	85	63.7	1.95	0.61	94	
	0800-0900					65.1	2.27	0.69	68	
	0900-1000					65.5	1.74	0.74	38	
	1000-1100					65.5	0.44	0.59	19	
	1600-1700					69.5	1.39	0.72	26	
	1700-1800					68.6	1.36	0.74	57	
	1800-1900	68.6	2.49	0.81	44	67.7	1.60	0.70	15	
	1900-2000	67.3	1.76	0.68	123	66.6	1.81	0.70	141	
	2000-2100	65.7	1.71	0.70	130	65.5	2.01	0.64	44	
	2100-2200	65.5	1.91	0.71	15					

results of the two studies, a correlation analysis was performed between Λ_p and VB_Z .

With $B_Z \geq 1$ nT

$$\Lambda_p = 2.09 - 0.91 VB_Z \quad (40)$$

86. Hardy, D. A., Christensen, M. S., Holman, T. J., Baple, W. L., and Heinemann, N. (1981) DAST/12 electron observations of equatorial auroral boundaries and their relationship to the solar wind velocity and the north-south component of the interplanetary magnetic field, J. Geophys. Res., 86, 9661.

with VB_Z in mV/m. This allows us to express the magnetospheric potential as a function of VB_Z .

$$\Phi(L, z) = \frac{1}{2} B_0 R_E^2 \left[(6.6 + 2.2 VB_Z) 10^{-4} L^2 \sin(z - z_0) - \frac{1}{L} \right] \quad (41)$$

To test the validity of this equation it is possible to calculate the cross-magnetospheric potential drop (Φ_m), and compare it with measured cross-polar-cap potential drops (Φ_{pc}).

To estimate Φ_m , we use the position and shape of the magnetopause in the equatorial plane given by McIlwain.⁸⁷ In this representation, the magnetopause lies at a distance of $11R_E$ near the subsolar point, and flares to a distance of $15R_E$ at the dawn-dusk meridian. We ignore storm-time compressions of the magnetosphere in the calculations. Two methods of calculating Φ_m are used. The first method sets $z_0 = 0$ in Eq. (40), making the axis of symmetry the dawn-dusk meridian. The second method uses empirical values of z_0 given in Figure 26. For $K_p = 0$, the axis is tilted with the dusk stagnation point 23° to the nightward side of the dawn-dusk meridian. For higher values of K_p , the stagnation point rotates sunward, reaching a constant value of -45° for $K_p \geq 2$. In Figure 27, we have sketched the axes of symmetry, indicating approximate distances to the dawn and dusk sides of the magnetopause for $K_p = 0, 1, 2$, and > 2 .

In Figure 28, Φ_m is plotted as a function of K_p , VB_Z , and B_Z . VB_Z is positive when the interplanetary electric field is directed from dawn to dusk (positive Y in standard geocentric, solar-magnetospheric coordinates). Values of B_Z are derived from VB_Z , using a solar wind speed of 400 km/sec. The solid line calculations assume $z_0 = 0$; that is, the dawn-dusk meridian is the axis of symmetry. For this case, Φ_m increases linearly from 6.5 kV for $K_p = 0$, to 65 kV for $K_p = 6$. The dot-dash line indicates values of Φ_m using empirical values of z_0 and axes of symmetry indicated in Figure 27. In these calculations, Φ_m ranges from 5.5 kV for $K_p = 0$, to 25 kV for $K_p = 6$. We note that in these calculations there is an abrupt transition in the trend of Φ_m near $K_p = 2$. This is close to our independently derived "breakpoint" in B_Z .

For reference, in Figure 28, we have also plotted average values of Φ_{pc} (dashed line) as a function of K_p based on two weeks of OGO-6 electric field measurements. Heppner⁶⁰ found that Φ_{pc} increased linearly from 20 kV for $K_p = 0$, to 100 kV at $K_p = 6$. At low values of K_p , the DMSF values of Φ_m are not sensitive

87. McIlwain, C. E. (1972) Plasma convection in the vicinity of geosynchronous orbit, in *Earth's Magnetospheric Processes*, B. M. McCormac, Ed., D. Reidel Co., Dordrecht, Holland, p. 267.

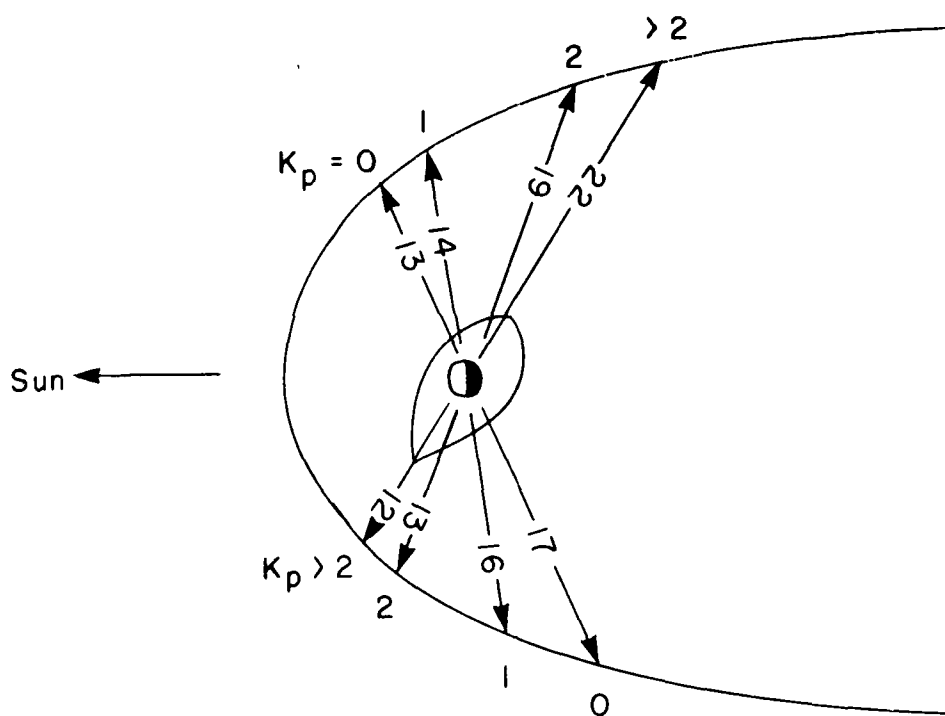


Figure 27. Equatorial Magnetopause⁴⁶ With Distances Along Axes of Symmetry for Various Values of K_p

to the value of ϕ_0 , and are considerably less than Heppner's $\Delta\phi_{pc}$. With values of $\phi_0 = -45^\circ$ for $K_p > 2$, ϕ_m and ϕ_{pc} are of comparable magnitudes. In a time average sense, ϕ_{pc} and ϕ_m are coupled through the process of magnetic reconnection in the magnetotail. The two quantities must be roughly the same since, on average, the amount of magnetic flux transferred to the nightside magnetosphere must equal the amount being returned to the dayside magnetosphere.

We emphasize that these are "average" results in the sense that they represent least squares fits to the data. Heppner⁶⁰ pointed out that $\Delta\phi_{pc}$ frequently exceeds 100 kV during periods of high K_p . Similarly, in both DMSP boundaries, for cases of large negative B_z and high K_p respectively, the latitude of the boundary is often much lower than the average. Since such cases correspond to the Alfvén boundary being closer than average to the earth, they also correspond to potentials exceeding 100 kV.

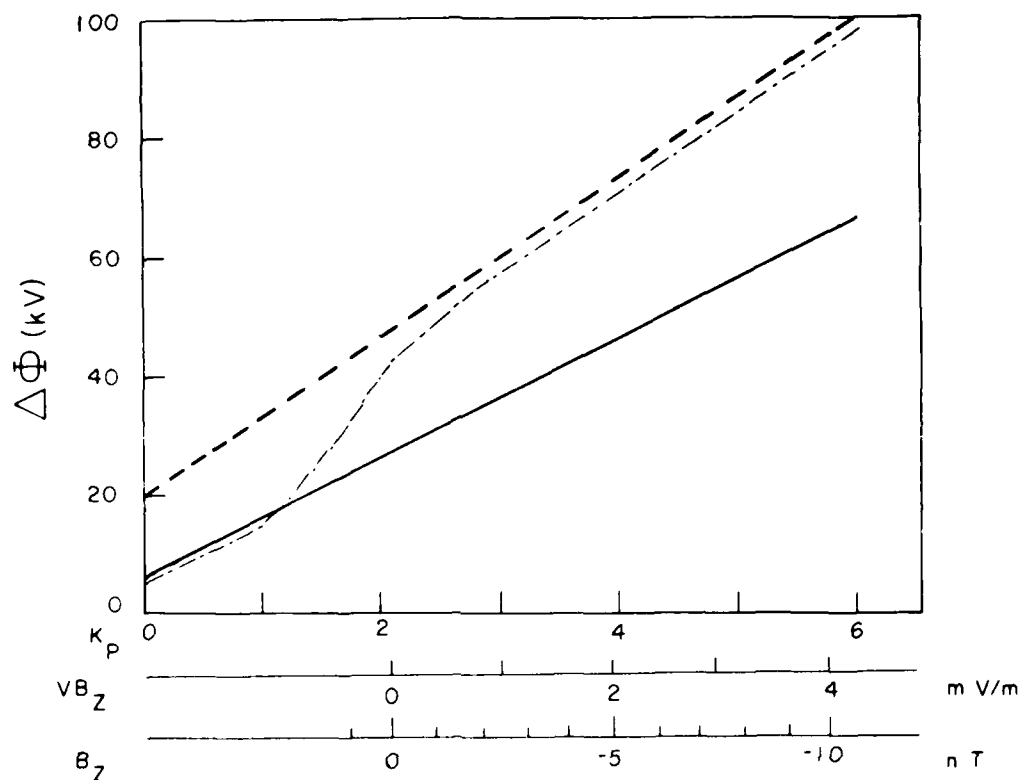


Figure 28. Polar Cap Potential, From Heppner⁶⁰ (Dashed Line), and From Eq. (12) With $z_0 = 0$ (Solid Line), and z_0 With Empirical Values (Dot-Dash Line)

7.3 Inverted-V Phenomenology

Diffuse auroral electron precipitation is fairly uniform, and isotropically distributed. In the poleward portion of the oval, electron fluxes are more spatially structured, and are often field aligned. Discrete, optical arcs are the most striking manifestation of the structuring process. The dominant structural features of electron fluxes observed with polar orbiting satellites are the so-called inverted-V structures. These structures are latitudinally narrow ($\sim 1^\circ$) bands of electron precipitation that increase in average energy from a few hundred eV to several keV, then return to a few hundred eV.⁸³ On energy-time spectrograms they have the shapes of inverted Vs. Although individual inverted-V structures have been

83. Frank, L. A., and Ackerson, K. L. (1971) Observations of charged particle precipitation into the auroral zone, *J. Geophys. Res.* 76:3612.

identified with ground-observed discrete arcs,⁸⁹ the general relationship between the two phenomena is not clear. Inverted-Vs have latitudinal dimensions of several hundred km, whereas optical arcs have typical widths of 1 to 10 km.⁹⁰

Lin and Hoffman⁹¹ have studied the global distribution of inverted-V structures, and the pitch-angle distribution of electrons within them. Figure 29 is an event occurrence map of 280 inverted-V structures observed with the AE-D satellite.

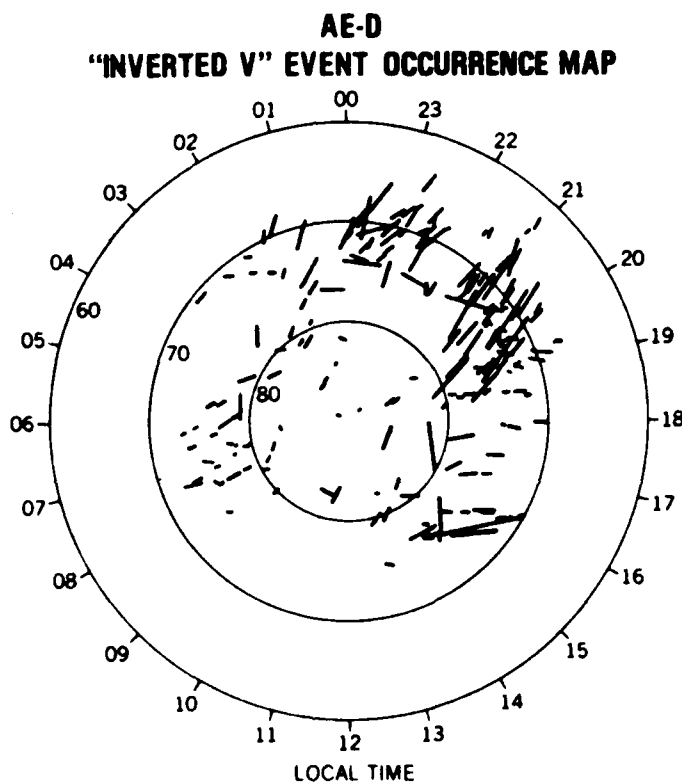


Figure 29. Spatial Occurrence Map of 280 Inverted-V Events. Local time and circles of constant invariant latitude are shown as reference

89. Ackerson, K. L., and Frank, L. A. (1972) Correlated satellite measurements of low-energy electron precipitation and ground-based observations of a visible auroral arc, J. Geophys. Res. 77:1128.
90. Maggs, J. E., and Davis, T. N. (1968) Measurement of the thickness of auroral structures, Planet. Space Sci. 16:205.
91. Lin, C. S., and Hoffman, R. A. (1979) Characteristics of the inverted-V event, J. Geophys. Res. 84:1514.

This map shows that inverted-Vs are found throughout the high-latitude region. They appear predominantly in the late evening sector, and are absent from the late pre-noon MLT sector.

The pitch-angle distribution of electrons measured over an inverted-V event is given in Figure 30. This spectrogram gives the ratio of field-aligned flux at a

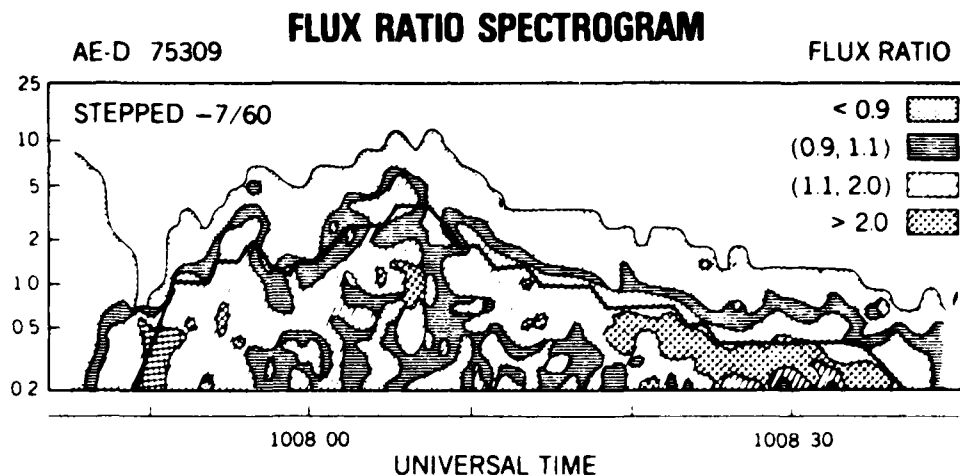


Figure 30. Spectrogram Displaying the Flux Ratios at 7° and 60° of an Inverted-V Event. The flux ratios are separated into four categories as shown in the upper right corner

given energy, to the flux at pitch angles of 60° . The heavy black line gives the energy at which the maximum differential flux was measured. Note that the energy of the peak flux rises to ~ 3 keV at 1008:05 UT then decreases to ~ 0.5 keV 20 seconds later. At the energy of the peak flux, the electrons are field-aligned, whereas those with higher energies are isotropic over the downcoming hemisphere. This distribution is consistent with the electrons having been accelerated through a field-aligned potential drop at an altitude above the point of observation.⁹² Electrons with energies less than that of the peak show highly complex pitch-angle distributions. Some of these electrons are secondaries and degraded primaries trapped between a magnetic mirror point and an electrostatic potential barrier. Some of the low-energy electrons are highly field-aligned, suggesting that they are

92. Evans, D. S. (1974) Precipitating electron fluxes formed by a magnetic field-aligned potential difference, *J. Geophys. Res.* 79:2853.

accelerated electrons of ionospheric origin. If so, the complexity of their distribution suggests that the field-aligned potential drop is varying temporally, and/or spatially.

One of the most exciting developments of the 1970s was the development of direct evidence for the existence of field-aligned potential drops from measurements by instrumentation on the S3-3 satellite. The observational work of the University of California, Berkeley group is summarized by Mozer.⁹³

The highly eccentric orbit of S3-3 carried it to altitudes of ~ 8000 km above the auroral ionosphere. This is a hitherto unexplored region. At these altitudes, very intense electric field structures were observed. An example given in Figure 31 shows electric fields at 8000 km reaching 400 mV/m, and undergoing

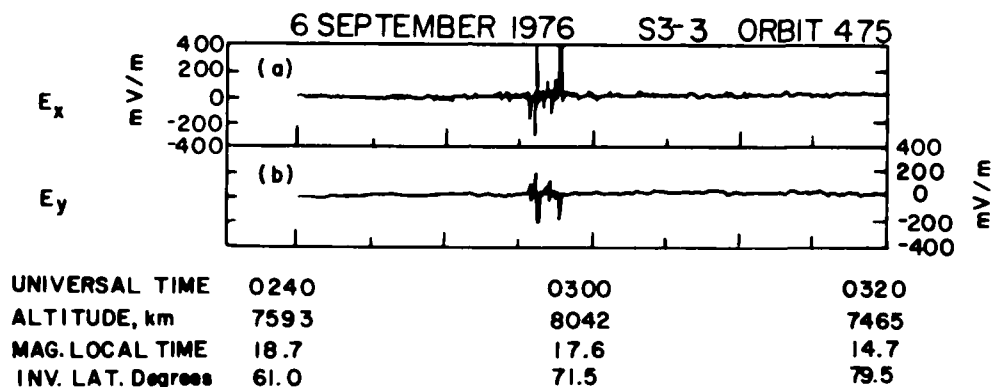


Figure 31. An Example of a Rapid Electric Field Reversal Observed at 8000 km by S3-3⁷⁸

rapid reversals. If mapped, assuming $\vec{E} \cdot \vec{B} = 0$, to auroral arc altitudes, the electric field intensities would be of the order of 1000 mV/m, and the latitudinal width of the structure would be < 10 km. This is a typical width of a discrete optical arc. The electric field intensity, however, greatly exceeds that measured in the lower ionosphere. For this reason, it is argued that there must be a potential drop along magnetic field lines that accelerate plasma sheet electrons to form arcs.

These electric field structures have been observed at all altitudes down to 1000 km. They are mostly found above 4000 km. Comparisons of S3-3 electric

93. Mozer, F. S. (1981) The low altitude electric field structure of discrete auroral arcs, in Physics of Auroral Arc Formation, S. -I. Akasofu, Ed., AGU Monograph 25, Washington, D. C., pp. 136-142.

field measurements with simultaneous measurements from other instruments on the spacecraft show that the electric field structures are embedded in regions of hydrogen cyclotron, electrostatic wave turbulence that are colocated with inverted-V precipitation structures. Within the electric field reversals, we find fluxes of field-aligned electrons going into, and H^+ and O^+ ions going out of, the ionosphere. The specific morphology of these structures is still under active study. An understanding of how these structures extend up to altitudes of 25,000 km will be one of the first fruits of the Dynamics Explorer-A satellite, launched in the summer of 1981.

7.1 Substorms

No overview of high-latitude electrodynamics would be complete without some comment, no matter how cursory, on substorms. It is during substorms that the dynamic coupling between the magnetosphere and ionosphere is most striking. Despite intensive studies of substorm processes over the last fifteen years, the richness of the observations has made total agreement on what constitutes the essential elements of a substorm elusive.

The evolution of discrete auroral arcs in the late-evening sector as synopsized from all-sky camera data by Akasofu,⁹⁴ is given in Figure 32. Under pre-substorm conditions, homogeneous arcs extending for thousands of kilometers in the east-west direction are found in the oval, and sun-aligned arcs are found in the polar cap. Substorm onset is announced by a brightening of the most equatorward arc. The discrete arcs expand poleward, and westward-traveling surges develop in the evening sector. After expanding to some maximum latitude, the arcs slowly retreat toward their pre-substorm condition.

To resolve differences between various schools of thought, nine active investigators met in August 1978 to: (1) specify substorm signatures, and (2) unambiguously define words commonly (often differently) used to describe substorm processes.⁹⁵ Major points of agreement were:

- (1) During extended periods of northward IMF, the magnetosphere quiets and asymptotically approaches a ground state.
- (2) As the IMF turns southward, magnetospheric convection increases. This enhanced convection can exist for some time prior to substorm onset.

94. Akasofu, S. -I. (1964) The development of the auroral substorm, Planet. Space Sci. 12:273.

95. Rostoker, G., Akasofu, S. -I., Foster, J., Greenwald, R. A., Kamide, Y., Kawasaki, K., Lui, A. T. Y., McPherron, R. L., and Russell, C. T. (1980) Magnetospheric substorms -- definitions and signatures, J. Geophys. Res. 85:1663.

- (3) Substorm onset is signaled by an explosive increase in luminosity of the most equatorward arc, an intensification of the auroral electrojet, and a burst of micropulsation. The burst of micropulsation testifies to the explosive nature of the onset process in the magnetospheric source region.
- (4) The expansion phase occurs from onset to the time when the midnight sector arcs have undergone their most poleward excursions. Note that, in this definition, multiple intensifications of the substorm process, each marked by a micropulsation burst, are allowed.
- (5) The recovery phase coincides with the period in which midnight sector arcs retreat equatorward.

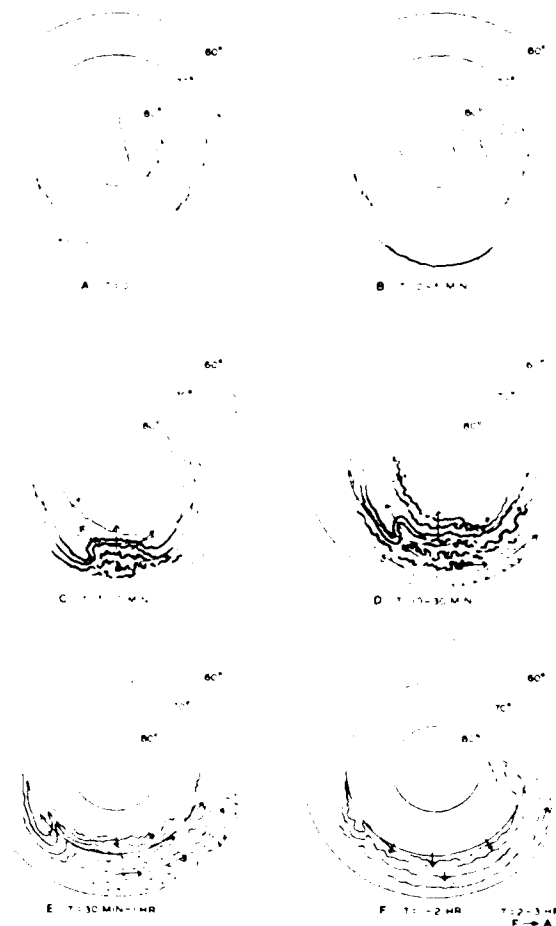


Figure 32. Schematic Diagram to Illustrate the Development of the Auroral Substorm. The center of the concentric circles in each stage is the north geomagnetic pole, and the sun is toward the top of the diagram

The substorm signatures dealt with in the August 1978 meeting are observable from ground-based instrumentation. Except for the micropulsation bursts, the signatures are of ionospheric effects whose causes lie in the magnetosphere. A key observation for understanding how substorms may be triggered comes from numerous satellites at geostationary altitude. During pre-substorm periods the nightside magnetic field at $6.7 R_E$ takes on a tail-like configuration. At substorm onset, the magnetic field rapidly recovers its normal, nearly dipolar, configuration. Simultaneously, hot plasma sheet particles, with no dispersion, are injected.

To explain the observations, the following scenario has been pieced together.

- (1) At a southward turning of the IMF, magnetic flux is transferred from the day to the night side of the magnetosphere. This process proceeds for about half an hour in which potential energy, in the form of stored magnetic flux, builds up in the tail. During this period, the neutral sheet current moves earthward to $\sim 10 R_E$ leading to a tail-like field geometry at $6.7 R_E$. Recall that discrete arcs map to the boundary plasma sheet, rather than the central plasma sheet. Thus, the most equatorward arc maps to a region near the inner edge of the neutral sheet current.
- (2) At substorm onset, the neutral sheet current near the inner edge of the boundary plasma sheet is diverted via field-aligned currents through the ionosphere. This leads to a collapse of the inner portion of the tail. In the ionosphere, part of the energy released in the collapse of the tail appears as an explosive brightening of the most equatorward arc. As the inner-tail field lines snap back to dipolar, plasma sheet electrons are rapidly accelerated by inductive electric fields, and are injected to the vicinity of geostationary distance. The process continues while B_z remains southward.
- (3) When the IMF turns northward, the rate of flux transfer decreases abruptly. If the IMF maintains a northward component for considerable time, the potential energy stored in the tail is slowly dissipated, and the magnetosphere relaxes toward a "ground state."

8. CONCLUSIONS

This treatise provides an introductory summary of what is known about the electrodynamics of the magnetosphere, and the high-latitude ionosphere, prior to the launch of the Dynamics Explorer satellites. Our knowledge is an amalgam of theoretical models and in situ observations. In a qualitative sense, we are

able to explain the gross features of magnetospheric processes. For example, a set of MHD equations has been used successfully to calculate the equilibrium shape of the magnetopause.¹ However, the microphysics of how (if) magnetic merging occurs at the magnetopause, and how particles cross the magnetopause to form the boundary layer, are not yet understood. An essentially MHD model for coupling between the ionosphere and magnetosphere⁴⁴ has been applied to successfully simulate substorm effects in the inner plasma sheet, and the low-latitude portion of the auroral oval.^{46,47} Thus, adiabatic energization is an important and well-understood magnetospheric process. Other energization processes, associated with reconnection in the magnetotail, are not understood. The role of parallel electric fields for the formation of auroral arcs was experimentally established in the 1970s. Competing theoretical models of how parallel electric fields form in a collisionless plasma fill the literature. The list of particle successes could go on and on.

With the gift of hindsight, it is interesting to examine the work of cartographers from the mid-seventeenth century. The mixed fruits of explorations spanning two hundred years are evident. Europe, the Middle East, Africa, and the eastern shores of the Americas are mapped with exquisite detail. Shapes assigned to the American west coasts and to the nations of east Asia range from vague to fanciful. Our own position, twenty years into the age of satellite exploration, is analogous to that of seventeenth-century map-makers. Some parts of the magnetosphere-ionosphere system are well explored. Our understanding of other important parts is based on fragmentary data samples, and leaves much to be desired. Undoubtedly, readers a few decades hence will find many of our ideas as quaintly amusing as the seventeenth-century image of Japan. To those who view cartography or space physics as quasi-static processes, this is a scandalous situation. To those involved in the process, it is the excitement of exploration.

SYMBOLS AND GLOSSARY

\vec{A}	Magnetic Vector potential
Mfven layer	(zero energy) Boundary between open and closed electric equipotentials in the magnetosphere. It is believed to mark the earthward boundary of the plasma sheet.
Auroral Oval	The instantaneous location of auroral particle precipitation
Beams	Accelerated, upward moving-ions observed at altitudes > 4000 km above auroral arcs with maximum fluxes along the magnetic field vector.
B	Magnetic Field
B_D	Dipole magnetic field of the earth
B_M	Magnetic Field strength at mirror point
B_{MT}	Magnetic Field strength in magnetotail
B_p	Total magnetic field at magnetopause
Conics	Accelerated ionospheric ions that are frequently observed at altitudes > 2000 km moving up auroral magnetic field lines with maximum fluxes at pitch angles between 0° and 90° .
Diffuse aurora	Relatively uniform precipitation of electrons and protons from central plasma sheet.
Double layer	A spatially confined region of potential drop frequently observed in laboratory plasmas. They are possibly responsible for field-aligned potential drops that occur above auroral arcs.
	Total energy of a particle
Res	Energy needed for a particle to undergo resonant scattering
E	Electric Field
E_C	Convective electric field
E_ω	Corotation electric field
Entry Layer	Alternate name for the interior cusp where magnetosheath electrons gain diffuse entry to the magnetosphere
Harang discontinuity	The boundary in the midnight sector between the westward and eastward electrojets
I	Height integrated current
IMF	Interplanetary magnetic field

Inverted-V	Latitudinally narrow ($\sim 1.0^\circ$) bands of electron precipitation that increase in average energy from a few hundred eV to several keV and then return to a few hundred eV. On time-energy spectrograms they have the shape of inverted Vs.
J	$\oint p_{\parallel} ds$ - the longitudinal invariant of particle motion in a force field
\vec{j}	Current density
K_p	Planetary 3-hour index of magnetic activity compiled from a worldwide network of mid-latitude magnetometer stations
L	Distance from the center of the earth measured in earth radii
Low Latitude Boundary Layer	A thin ($\sim 0.5 R_E$) layer inside the magnetopause characterized by closed magnetic field lines and magnetosheath plasma flowing in the antisunward direction
\vec{M}	Magnetic moment vector of the earth
m_p	mass of a proton
Magnetosheath	Region of shocked solar wind plasma flow
L_S	R_S/R_E
\hat{n}_M	Unit normal, directed outward from magnetosphere
n_s	Solar wind density
P	Total pressure tensor
p_{se}	Thermal pressure due to solar wind electrons
p_{si}	Thermal pressure due to solar wind ions
Plasma mantle	A region of antisunward, field-aligned plasma flow observed inside the magnetosphere in the region of open magnetic field lines
Pitch Angle	The angle between a particle's velocity and the local magnetic field vector
Plasma Sheet Boundary Layer	A spatially thin region between the central plasma sheet and the lobes of the magnetotail. The region is often marked by significant field-aligned plasma flows
R	Radius of curvature of magnetic field lines
R_E	Earth Radius
R_{MT}	Radius of magnetotail
R_S	Distance to the stagnation point where corotation and convective electric fields cancel exactly
SE	Geocentric solar ecliptic coordinates
SM	Geocentric solar magnetospheric coordinates

T	Maxwell stress tensor
vB_z	Z component of interplanetary magnetic field multiplied by its velocity. This quantity is also referred to as the interplanetary electric field
v_C	Drift velocity due to magnetic field line curvature
v_D	Drift velocity
v_E	Drift velocity due to electric field
v_G	Drift velocity due to magnetic field gradient
v_n	Neutral wind velocity
v_s	Solar wind velocity
α	Pitch angle
α_{eq}	Pitch angle of a particle at the magnetic equator
α_L	Angle of atmospheric loss cone shaping factor
γ	Parameter giving the level of electrical shielding of the magnetosphere from the convective dawn-to-dusk electric field
ϵ	Parameter used by Akasofu, $vB^2 \sin^4 (\theta/2)$
Δ	Equatorward boundary of diffuse auroral precipitation (see Alfvén boundary)
μ	Magnetic moment
ϵ_0	Permittivity of free space
σ	Conductivity tensor
σ_p	Pedersen conductivity
Φ	Electrical potential
Φ_m	Cross-magnetospheric potential drop
Φ_{pc}	Cross-polar cap potential drop
l	Local time, angle measured from midnight
λ	Inclination of magnetic field lines
Ψ	$q \int \mathbf{V} \cdot d\mathbf{l}$ - the flux invariant of energetic particle motion
ω	Angular spin velocity of the Earth

References

1. Mead, G. D., and Beard, D. B. (1964) Shape of the geometric field solar wind boundary, J. Geophys. Res., **69**:1169.
2. Olson, W. P. (1969) The shape of the tilted magnetopause, J. Geophys. Res., **74**:5642.
3. Johnson, F. S. (1969) The gross character of the geomagnetic field in the solar wind, J. Geophys. Res., **65**:3049.
4. Piddington, J. H. (1963) Theories of the geomagnetic storm main phase, Planet. Space Sci., **11**:1277.
5. Gold, T. (1969) Motions in the magnetosphere of the earth, J. Geophys. Res., **64**:1219.
6. Axford, W. I., and Hines, C. O. (1961) A unifying theory of high-latitude geophysical phenomena and geomagnetic storms, Can. J. Phys., **39**:1436.
7. Dungey, J. W. (1961) Interplanetary magnetic field and the auroral zones, Phys. Rev. Lett., **6**:47.
8. Eastman, T. E., Hones, Jr., E. W., Bame, S. J., and Asbridge, J. R., (1976) The magnetospheric boundary layer: site of plasma momentum and energy transfer from the magnetosheath into the magnetosphere, Geophys. Res. Lett., **3**:635.
9. Russell, C. T., and Elphic, R. C. (1979) ISFT observations of flux transfer events at the dayside magnetopause, Geophys. Res. Lett., **6**:37.
10. Moret, F. S., Forbort, R. B., Falderson, L. V., Falthinsen, C. C., Gonfalone, A., Pedersen, A., and Russell, C. T. (1979) Direct observation of a tangential electric field component at the magnetopause, Geophys. Res. Lett., **6**:395.
11. Hasegawa, H., Paschmann, G., Schepke, N., Rosenbluth, M., and Tsurutani, B. T. (1979) The magnetopause current: location of the current region and the production of the ionization, J. Geophys. Res., **84**:1169.

12. Crooker, N. U. (1977) Dayside merging and cusp geometry, J. Geophys. Res. **82**:3629.
13. Crooker, N. U. (1979) The magnetospheric boundary layers: a geometrically explicit model, J. Geophys. Res. **84**:951.
14. Vasyliunas, V. M. (1979) Interaction between the magnetospheric boundary layers and the ionosphere, Proc. Magnetospheric Boundary Layers Conf. (ESA SP-148) Alpbach, Austria, p. 387.
15. Freeman, J. W. (1979) Internal magnetospheric plasma flow, Proc. Magnetospheric Boundary Layers Conf. (ESA SP-148) Alpbach, Austria, p. 351.
16. Rosenbauer, H., Grünwaldt, H., Montgomery, M. D., Paschmann, G., and Sekopke, N. (1975) HEOS 2 plasma observations in the distant polar magnetosphere: the plasma mantle, J. Geophys. Res. **80**:2723.
17. Sekopke, N., Paschmann, G., Rosenbauer, H., and Fairfield, D. H. (1975) Influence of the interplanetary magnetic field on the occurrence and thickness of the plasma mantle, J. Geophys. Res. **81**:2687.
18. Hardy, D. A., Hills, H. K., and Freeman, J. W. (1975) A new plasma regime in the distant geomagnetic tail, Geophys. Res. Lett. **2**:169.
19. Pilipp, W. G., and Morfill, G. (1978) The formation of the plasma sheet resulting from plasma mantle dynamics, J. Geophys. Res. **83**:5670.
20. Sekopke, N., Paschmann, G., Haerendel, G., Sonnerup, B. U. Ö., Bame, S. J., Forbes, T. G., Hones, Jr., E. W., and Russell, C. T. (1981) Structure of the low-latitude boundary layer, J. Geophys. Res. **86**:2099.
21. Eastman, T. E., and Hones, Jr., E. W. (1979) Characteristics of the magnetospheric boundary layer and magnetopause layer as observed by IMP 6, J. Geophys. Res. **84**:2019.
22. Lemaire, J., and Roth, M. (1978) Penetration of solar wind plasma elements into the magnetosphere, J. Atmos. Terr. Phys. **10**:231.
23. Frank, L. A., Ackerson, K. L., and Lepping, F. P. (1976) On hot tenuous plasmas, fireballs and boundary layers in the earth's magnetotail, J. Geophys. Res. **81**:5859.
24. Gringauz, I. I., Bezrukhikh, V. V., Ozerov, V. D., and Ruzhinskii, E. E. (1961) A study of the interplanetary ionized gas, high energy electrons, and corpuscular radiation from the sun by means of the three-electrode trap for charged particles on the second Soviet cosmic rocket, Sov. Phys.-Dokl. **5**:361.
25. Vasyliunas, V. M. (1972) Magnetospheric Plasma, in Solar Terrestrial Physics, E. Dyer, Ed., D. Reidel Co., Dordrecht, Holland, p. 192.
26. Vasyliunas, V. M. (1968) A survey of low-energy electrons in the evening sector of the magnetosphere with OGO-1 and OGO-3, J. Geophys. Res. **73**:2379.
27. Frank, L. A. (1971) Relationship of the plasma sheet, ring current, trapping region, and plasma pause near the magnetic equator and local midnight, J. Geophys. Res. **76**:2269.
28. Hones, Jr., E. W., Stribling, J. R., Bame, S. J., Montgomery, J. D., and Singer, S. (1973) Substorm variations of the magnetotail plasma sheet from $N_{SM} = +6 R_E$ to $N_{SM} = -60 R_E$, J. Geophys. Res. **78**:109.
29. Rich, F. J., Rees, D. L., and Burke, W. J. (1973) Plasma sheet and lunar distance characteristics and interactions with the lunar surface, J. Geophys. Res. **78**:3097.

30. Speiser, T. W. (1967) Particle trajectories in model current sheets, II: Application to auroras using a geomagnetic tail model, J. Geophys. Res. 72:3919.
31. TerHaar, D. (1964) Elements of Hamiltonian Mechanics, North Holland Co., Amsterdam, Ch. 6.
32. Northrop, T. G. (1963) The Adiabatic Motion of Charged Particles, Interscience, New York, Ch. 3.
33. Rossi, B., and Olbert, S. (1970) Introduction to the Physics of Space, McGraw-Hill, New York, Ch. 5.
34. Hines, C. O. (1963) The energization of plasma in the magnetosphere: hydro-magnetic and particle drift approaches, Planet. Space Sci. 10:239.
35. Kivelson, M. G., Kave, S. M., and Southwood, D. J. (1979) The physics of plasma injection events, in Dynamics of the Magnetosphere, S.-I. Akasofu, Ed., D. Reidel Co., Hingham, Massachusetts, p. 385.
36. Ejiri, M., Hoffman, R. A., and Smith, P. H. (1978) The convection electric field model for the magnetosphere based on Explorer 45 observations, J. Geophys. Res. 83:4811.
37. Gussenhoven, M. S., Hardy, D. A., and Burke, W. J. (1981) DMSP/F2 electron observations of equatorward auroral boundaries and their relationship to magnetospheric electric fields, J. Geophys. Res. 86:768.
38. Southwood, D. J., and Kaye, S. M. (1979) Drift boundary approximations in simple magnetospheric convection models, J. Geophys. Res. 84:5773.
39. Kennel, C. F., and Petschek, H. E. (1966) Limit on stably trapped particle fluxes, J. Geophys. Res. 71:1.
40. Williams, D. J., and Lyons, L. R. (1974) The proton ring current and its interaction with the plasmapause: storm recovery phase, J. Geophys. Res. 79:4195.
41. Gurnett, D. A., and Frank, L. A. (1977) A region of intense plasma wave turbulence on auroral field lines, J. Geophys. Res. 82:1031.
42. Young, T. S. T., Callen, J. D., and McCune, J. E. (1973) High frequency electrostatic waves in the magnetosphere, J. Geophys. Res. 78:1082.
43. Ashour-Abdalla, M., and Thorne, R. M. (1978) Toward a unified view of diffuse auroral precipitation, J. Geophys. Res. 83:4755.
44. Vasylunas, V. M. (1970) Mathematical models of magnetospheric convection and its coupling to the ionosphere, in Particles and Fields in the Magnetosphere, B. M. McCormac, Ed., D. Reidel Co., Dordrecht, Holland, p. 60.
45. Lyons, L. R., Evans, D. S., and Lundin, R. (1979) An observed relationship between magnetic field aligned electric fields and downward electron energy fluxes in the vicinity of auroral forms, J. Geophys. Res. 84:457.
46. Harel, M., Wolf, R. A., Reiff, P. H., Spiro, R. W., Burke, W. J., Rich, F. J., and Smiddy, M. (1981) Quantitative simulation of a magnetospheric substorm, 1, model logic and overview, J. Geophys. Res. 86:2217.
47. Harel, M., Wolf, R. A., Spiro, R. W., Reiff, P. H., Burke, W. J., Rich, F. J., and Smiddy, M. (1981) Quantitative simulation of a magnetospheric substorm, 2, comparison with observations, J. Geophys. Res. 86:2242.
48. Fableson, U. V. (1967) Theory of electric field measurements conducted in the magnetosphere with electric probes, Space Sci. Rev. 7:238.

49. Hanson, W. B., and Heelis, R. A. (1975) Techniques for measuring bulk gas motions from satellites, Space Sci. Inst. 1:493.
50. Armstrong, J., and Zmuda, A. J. (1973) Triaxial magnetic measurements of field aligned currents at 800 km in the auroral region: initial results, J. Geophys. Res. 78:6802.
51. Frank, L. A. (1967) Initial observations of low-energy electrons in the earth's magnetosphere with OGO-3, J. Geophys. Res. 72:185.
52. Smiddy, M., Burke, W. J., Kelley, M. C., Saflekos, N., Gussenhoven, M. S., Hardy, D. A., and Rich, F. J. (1980) Effects of high latitude conductivity on observed convection electric fields and Birkeland currents, J. Geophys. Res. 85:6811.
53. Rostoker, G. (1980) Magnetospheric and ionospheric currents in the polar cap and their dependence on the B_y component of the interplanetary magnetic field, J. Geophys. Res. 85:4167.
54. Heppner, J. P. (1972) Polar cap electric field distributions related to the interplanetary magnetic field direction, J. Geophys. Res. 77:4877.
55. Friis-Christensen, E., Lassen, K., Willjelm, J., Wilcox, J. M., Gonzalez, W., and Colburn, D. S. (1972) Critical component of the interplanetary magnetic field responsible for large geomagnetic events, J. Geophys. Res. 77:3371.
56. Burke, W. J., Kelley, M. C., Sagalyn, R. C., Smiddy, M., and Lai, S. T. (1979) Polar cap electric field structure with a northward interplanetary magnetic field, Geophys. Res. Lett. 6:21.
57. Russell, C. T. (1972) The configuration of the magnetosphere, in Critical Problems of Magnetospheric Physics, E. R. Dyer, Ed., National Academy of Science, Washington, D. C., p. 1.
58. Maezawa, K. (1976) Magnetospheric convection induced by the positive and negative Z components of the interplanetary magnetic field: quantitative analysis using polar cap magnetic records, J. Geophys. Res. 81:2289.
59. Podgorny, I. M., Dubinin, E. M., and Potanin, Yu. N. (1978) The magnetic field on the magnetospheric boundary from laboratory simulation data, Geophys. Res. Lett. 4:207.
60. Heppner, J. P. (1977) Empirical models of high-latitude electric fields, J. Geophys. Res. 82:1115.
61. Reiff, P. H., Spiro, R. W., and Hill, T. W. (1981) Dependence of polar-cap potential drop on interplanetary parameters, J. Geophys. Res. 86:7639.
62. Akasofu, S.-I. (1978) Interplanetary energy flux associated with magnetospheric substorms, Planet. Space Sci. 27:425.
63. Hill, T. W. (1979) Generation of the magnetospheric electric field, in Quantitative Modelling of Magnetospheric Processes, W. P. Olson, Ed., AGU Monograph 21, Washington D. C., p. 297.
64. Winningham, J. D., and Heikkila, W. J. (1974) Polar cap auroral electron fluxes observed with Isis 1, J. Geophys. Res. 79:949.
65. Meng, C.-I., and Kroel, H. W. (1977) Intense uniform precipitation of low-energy electrons over the polar cap, J. Geophys. Res. 83:2305.
66. Yaeger, D. M., and Frank, L. A. (1976) Low energy electron intensities at large distances over the earth's polar cap, J. Geophys. Res. 81:3966.
67. Meng, C.-I., Akasofu, S.-I., and Anderson, K. A. (1977) Dawn-dusk gradient of the precipitation of low-energy electrons over the polar cap and its relation to the interplanetary magnetic field, J. Geophys. Res. 82:271.

68. Foster, J. C., and Burrows, J. R. (1976) Electron fluxes over the polar cap 1, intense keV fluxes during poststorm quieting, J. Geophys. Res. **81**:6016.
69. Foster, J. C., and Burrows, J. R. (1977) Electron fluxes over the polar cap 2, electron trapping and energization on open field lines, J. Geophys. Res. **82**:5165.
70. Ismail, S., Wallis, D. D., and Cogger, L. L. (1977) Characteristics of polar sun-aligned arcs, J. Geophys. Res. **82**:4741.
71. Weber, E. J., and Buchau, J. (1981) Polar cap F-layer auroras, Geophys. Res. Lett. **8**:125.
72. Eather, R. H. (1979) DMSP calibration, J. Geophys. Res. **84**:4134.
73. Hardy, D. A., Burke, W. J., and Gussenhoven, M. S. (1981) DMSP optical and electron measurements in the vicinity of polar cap arcs, J. Geophys. Res. **87**:2413.
74. Burch, J. T., Fields, S. A., and Heelis, R. A. (1979) Polar cap electron acceleration regions, J. Geophys. Res. **84**:5863.
75. Burke, W. J., Gussenhoven, M. S., Kelley, M. C., Hardy, D. A., and Rich, F. J. (1982) Electric and magnetic field characteristics of discrete arcs in the polar cap, J. Geophys. Res. **87**:2431.
76. Lyons, L. R. (1980) Generation of large-scale regions of auroral currents, electric potentials, and precipitation by the divergence of the convection electric field, J. Geophys. Res. **85**:17.
77. Lyons, L. R. (1981) Discrete aurora as the direct result of an inferred high-altitude generating potential distribution, J. Geophys. Res. **86**:1.
78. Mozer, F. S., Cattell, C. A., Hudson, M. K., Lysak, R. L., Temerin, M., and Forber, R. B. (1980) Satellite measurements and theories of low altitude auroral particle acceleration, Space Sci. Rev. **27**:155.
79. Iijima, T., and Potemra, T. A. (1978) Large-scale characteristics of field aligned currents associated with substorms, J. Geophys. Res. **83**:599.
80. Klumpar, D. M. (1979) Relationships between auroral particle distributions and magnetic field perturbations associated with field aligned currents, J. Geophys. Res. **84**:6524.
81. Maynard, N. C. (1974) Electric field measurements across the Harang discontinuity, J. Geophys. Res. **79**:4620.
82. McDiarmid, J. B., Burrows, J. R., and Wilson, M. D. (1979) Large-scale magnetic field perturbations and particle measurements at 1400 km on the dayside, J. Geophys. Res. **84**:1431.
83. Doyle, M. A., Rich, F. J., Burke, W. J., and Smiddy, M. (1981) Field aligned currents and electric fields in the region of the dayside cusp, J. Geophys. Res. **86**:5656.
84. Fairfield, D. H., and Mead, G. D. (1975) Magnetospheric mapping with a quantitative geomagnetic field model, J. Geophys. Res. **80**:535.
85. Mauk, B. H., and McIlwain, C. E. (1974) Correlations of K_p with substorm injected plasma boundary, J. Geophys. Res. **79**:3193.

86. Hardy, D. A., Gussenhoven, M. S., Holman, E., Burke, W. J., and Heinemann, N. (1981) DMSP/F2 electron observations of equatorial auroral boundaries and their relationship to the solar wind velocity and the north-south component of the interplanetary magnetic field, J. Geophys. Res. 86:9961.
87. McIlwain, C. E. (1972) Plasma convection in the vicinity of geosynchronous orbit, in Earth's Magnetospheric Process, B. M. McCormac, Ed., D. Reidel Co., Dordrecht, Holland, p. 268.
88. Frank, L. A., and Ackerson, K. L. (1971) Observations of charged particle precipitation into the auroral zone, J. Geophys. Res. 76:3612.
89. Ackerson, K. L., and Frank, L. A. (1972) Correlated satellite measurements of low-energy electron precipitation and ground-based observations of a visible auroral arc, J. Geophys. Res. 77:1128.
90. Maggs, J. E., and Davis, T. N. (1968) Measurement of the thickness of auroral structures, Planet. Space Sci. 16:205.
91. Lin, C. S., and Hoffman, R. A. (1979) Characteristics of the inverted-V event, J. Geophys. Res. 84:1514.
92. Evans, D. S. (1974) Precipitating electron fluxes formed by a magnetic field-aligned potential difference, J. Geophys. Res. 79:2853.
93. Mozer, F. S. (1981) The low altitude electric field structure of discrete auroral arcs, in Physics of Auroral Arc Formation, S.-I. Akasofu, ed., AGU Monograph 25, Washington, D. C., pp.136-142.
94. Akasofu, S.-I. (1964) The development of the auroral substorm, Planet. Space Sci. 12:273.
95. Rostoker, G., Akasofu, S.-I., Foster, J., Greenwald, R. A., Kamide, Y., Kawasaki, K., Lui, A. T. Y., McPherron, R. L., and Russell, C. T. (1980) Magnetospheric substorms—definitions and signatures, J. Geophys. Res. 85:1663.

